RESEARCH ARTICLE | NOVEMBER 26 2025

Pressure calibrations of high-pressure large-volume presses at HPSTAR

Special Collection: High Pressure Science 2026

Yongjiang Xu (徐永江) ; Peiyan Wu (吴培衍) ; Sheng Shang (尚升) ; Xue Wang (王雪) ; Taihang Li (李钛航) ; Shuchang Gao (高书畅) ; Shijie Lv (吕世杰) ; Hang Cheng (程行); Qianzhi Xu (许潜智) ; Shang Lei (雷尚) ; Jiajia Feng (冯嘉嘉) ; Lei Zhao (赵磊); Wim van Westrenen ; Takayuki Ishii (石井 貴之) ; Bin Chen (陈斌) ; Lei Su (苏磊); Yang Ding (丁阳) ; Wenge Yang (杨文革) ; Ho-Kwang Mao (毛河光) ; Yanhao Lin (林彦蒿)

Matter Radiat. Extremes 11, 017803 (2026)
https://doi.org/10.1063/5.0289378

Matter and Radiation at Extremes | RESEARCH ARTICLE | pubs.aip.org/aip/mre

Pressure calibrations of high-pressure large-volume presses at HPSTAR

Cite as: Matter Radiat. Extremes 11, 017803 (2026); doi: 10.1063/5.0289378
Submitted: 7 July 2025 • Accepted: 23 October 2025 •
Published Online: 26 November 2025

Yongjiang Xu (徐永江),[1] Peiyan Wu (吴培衍),[1] Sheng Shang (尚升),[1] Xue Wang (王雪),[1] Taihang Li (李钛航),[1] Shuchang Gao (高书畅),[1,2] Shijie Lv (吕世杰),[1,3] Hang Cheng (程行),[1] Qianzhi Xu (许潜智),[1] Shang Lei (雷尚),[1] Jiajia Feng (冯嘉嘉),[1] Lei Zhao (赵磊),[1] Wim van Westrenen,[1,4] Takayuki Ishii (石井 貴之),[1,5] Bin Chen (陈斌),[1] Lei Su (苏磊),[1,3] Yang Ding (丁阳),[1] Wenge Yang (杨文革),[1] Ho-Kwang Mao (毛河光),[1,3] and Yanhao Lin (林彦蒿)[1,a)]

AFFILIATIONS

[1] Center for High Pressure Science and Technology Advanced Research, Beijing 100193, China
[2] Earth and Environmental Sciences, KU Leuven, 3001 Leuven, Belgium
[3] Shanghai Advanced Research in Physical Sciences, Shanghai 201203, China
[4] Department of Earth Sciences, Faculty of Science, Vrije Universiteit Amsterdam, De Boelelaan, 1100 Amsterdam, The Netherlands
[5] Institute for Planetary Materials, Okayama University, Misasa 6820193, Japan

Note: Paper published as part of the Special Topic on High Pressure Science 2026.
[a)] **Author to whom correspondence should be addressed:** yanhao.lin@hpstar.ac.cn

ABSTRACT

Large-volume presses (LVPs) are widely utilized in diverse research fields—including high-pressure physics, chemistry, materials science, and Earth and planetary sciences—to investigate the physical and chemical properties of materials under extreme high-pressure and high-temperature conditions. A prerequisite for achieving reproducible property measurements is the determination and control of pressure within experimental setups. However, the lack of precise pressure calibration in LVPs hinders the broader application of such devices in ultrahigh-pressure studies. This study employs a suite of standard phase transition-based pressure markers—comprising metallic conductors, semiconductors, and minerals—through both *in situ* and *ex situ* identification approaches, to establish pressure calibration curves ranging from 0.4 to >30 GPa for various types of LVP installed at the Center for High Pressure Science and Technology Advanced Research (HPSTAR), Beijing, including piston–cylinder, cubic, and multi-anvil presses. The results provide a unified and traceable pressure reference for high-pressure experiments conducted at HPSTAR, while also offering technical guidance and calibration standards for other researchers utilizing similar LVP systems, thereby enabling more consistent comparison between different laboratories. This work facilitates the advancement of LVP research toward broader applications in higher-pressure regimes.

I. INTRODUCTION

High-pressure experimentation has opened a new window for exploring material properties under extreme pressure and temperature conditions,[1] and it continues to yield new discoveries in high-pressure physics, chemistry, materials science, and Earth and planetary sciences.[2–16] The synthesis of materials under high-pressure and high-temperature conditions using large-volume presses (LVPs) provides a unique way to help identify new phases, structures, and chemical reactions and to measure their properties.[17–20]

Commonly used LVPs include piston–cylinder presses,[21,22] six-anvil cubic presses,[23] and multi-anvil presses,[24–29] which can generate pressures ranging from below one gigapascal to tens of gigapascals.[30–42] In geoscience, this is equivalent to conditions from the crust to the lower mantle in the Earth's interior.

Pressure determination is an essential step in performing accurate and precise high-pressure experiments. When quantum beams such as synchrotron X-ray and neutron radiation are available, sample pressure can be determined during experiments based on unit cell volume changes of pressure-standard materials such as

crystalline NaCl, Au, and MgO.[43–45] However, most high-pressure experiments are performed without quantum beams in a laboratory, where pressure against press load needs to be calibrated. This is necessary because of the complex nonlinear responses of different assembly materials to applied pressure and temperature, and because of differences in the designs of the presses themselves and the materials used to construct them.[46] Pressure calibration is achieved by identifying changes in the properties of standard calibration materials that are known to occur at pressures and temperatures determined using an independent technique.[31,35,39,40,42,47] Precise pressure calibration is important not only for synthesizing materials in materials science, but also for linking measurements in experimental setups with "real life" observations of properties at high pressure (for example, high-pressure phase transitions in planetary science that are observed by seismological studies), and to be able to quantify targeted improvements to the development of high-pressure techniques, for example, by aiming to extend techniques to higher pressures.

Unfortunately, in many cases, primary calibration information of LVP devices is poorly documented, inaccessible, or altogether missing from the scientific literature. Here, we provide detailed information about the structure and materials used in high-pressure assemblies, the range of pressure calibrants used, and quantitative descriptions of the resulting pressure calibration curves for nine LVPs at the Center for High Pressure Science and Technology Advanced Research (HPSTAR), Beijing, including piston–cylinder presses, six-anvil cubic presses, and multi-anvil presses. Our aim is to provide a consistent reference dataset for the use of these assemblies and devices, as well as a baseline for comparison with other LVP setups using similar assemblies, and with new assembly designs replacing the current setups.

II. OVERVIEW OF EXPERIMENTAL SETUPS

To date, nine high-pressure LVPs of piston–cylinder, cubic, and multi-anvil designs have been installed and thoroughly pressure-calibrated at HPSTAR. A summary of these LVPs, including their manufacturers, nominal maximum forces, cylinder bore diameters, and highest pressures calibrated to date, is presented in Table I.

All of the materials used in the cell assemblies studied here were obtained from specific suppliers and manufacturers or customized from various factories in China, as detailed in Table II. This list facilitates future efforts to ensure material consistency and to define the range of material properties suitable for high-pressure research.

III. METHODOLOGY: PRESSURE CALIBRATION STRATEGY

A. Overview

Pressure calibration of high-pressure apparatus relies on detecting changes in the physical or chemical properties of selected reference materials under known pressure conditions. Calibration is often initially performed under room temperature conditions. Because many studies in materials science and geoscience focus on high-temperature processes, room-temperature calibrations are

TABLE I. Summary of calibrated LVPs at HPSTAR. Note: all of these conversions use the relationships 1 ton-force (metric) = 0.009 806 65 MN and 1 bar = 10^5 Pa.

High-pressure apparatus	Nominal maximum force (MN)	Cylinder bore diameter (mm)	Manufacturer	Calibrated pressure range (GPa)
Piston–cylinder press:				
RTK-PC-II	2.5	216	Hubei Rocktek Instrument Co., Ltd.	0.4–3.14
Cubic presses:				
MP280	6 × 6	280	Guilin MPa Machinery Technology Co., Ltd.	2.55–7.6
GY420-A	6 × 14	420	Guilin Guiye Machinery Co., Ltd.	2.55–4.5
GY420-B	6 × 14	420	Guilin Guiye Machinery Co., Ltd.	2.55–5.55
GY560	6 × 27	560	Guilin Guiye Machinery Co., Ltd.	2.55–7.6
Multi-anvil presses:				
Kawai (split-sphere)-type RTK-WC1000	10	432	Hubei Rocktek Instrument Co., Ltd.	2.55–29.2
Kawai (split-sphere)-type LPRU1500	15	600[a]	Max Voggenreiter GmbH	2.55–30.6
Kawai (split-sphere)-type LPRU2000	20	596[b]	Max Voggenreiter GmbH	2.55–22.2
Osugi (DIA)-type LPRU1500	15	540[c]	Max Voggenreiter GmbH	2.55–22.2

[a]Approximate cylinder bore diameter calculated using conversion factor from product manual: 1 ton-force = (oil pressure in bars) × 2.8822.
[b]Approximate cylinder bore diameter calculated using conversion factor from product manual: 1 ton-force = (oil pressure in bars) × 2.842.
[c]Approximate cylinder bore diameter calculated using conversion factor from product manual: 1 ton-force = (oil pressure in bars) × 2.334.

TABLE II. List of materials for cell assemblies.

Apparatus	Component	Material	Manufacturer/supplier	Product Id.
Piston–cylinder press	Talc tube	Talc		
	Glass tube	Pyrex glass		
	Steel cap	Steel		
	Heater	Graphite	Customized	...
	Pyrophyllite ring	South African black pyrophyllite		
	Four-hole alumina tube	Al_2O_3 ceramic		
Cubic press	Pyrophyllite briquetted	Mentougou yellow pyrophyllite	Liaocheng Xinke Pyrophyllite Co., Ltd.	
	Sleeve	Semisintered MgO	Max Voggenreiter GmbH	...
	Molybdenum disk	Molybdenum		
	Secondary anvil	YG8 tungsten carbide	Customized	
	Heater	Graphite		
Multi-anvil press	Octahedron	Cr_2O_3-doped sintered MgO	Mino Ceramics Co., Ltd.	OM-CR
	Octahedron	CoO-doped sintered MgO		OM-CO
	Thermo-insulator	CaO-doped sintered ZrO_2		OZ-8C-HD
	Heater	Cr_2O_3, Al_2O_3, and SrO-doped $LaCrO_3$		S6
	Heater	Rhenium	China Rhenium Co., Ltd.	
	Sleeve	Semisintered MgO	Max Voggenreiter GmbH	...
	Gasket	South African black pyrophyllite	Customized	

TABLE III. Pressure calibration reference points recommended in this study.

P (GPa)	Temperature[a]	Material	Transition[b]	Refs.
2.55[c]	R.T.	Bi	I–II	54
4		Cd_3P_2	I–II	55
5.55		Ba	I–II	56
7.6		Bi	III–V	57
13.3		ZnSe	ZB–RS	58
13.7[d]		Pb	I–II	59
17.3		GaAs	ZB–*Cmcm*	60
22.2		GaP	ZB–*Cmcm*	61
29.2		Te	III–V	62
Equations				
$T(^\circ\mathrm{C}) = 800.6 + 21.155P - 0.03736P^2 - 10.4P^3 + 2.4P^4$ (P in kbar)	H.T.	NaCl	Melting	63
$P(\mathrm{kbar}) = 21.945 + 0.006\,901[T(^\circ\mathrm{C}) + 273]$		SiO_2	Qz/Cs	47
$P(\mathrm{GPa}) = 4.7 + 0.0031[T(^\circ\mathrm{C}) + 273]$		SiO_2	Cs/St	64
$P(\mathrm{GPa}) = 0.5 + 0.0034T(\mathrm{K})$		Fe_2SiO_4	Fa/Ah	65
$P(\mathrm{GPa}) = 7.8 + 0.004[T(^\circ\mathrm{C}) + 273]$[e]		Mg_2SiO_4	Fo/Wd	66
$P(\mathrm{GPa}) = 13.1 + 0.00411[T(^\circ\mathrm{C}) + 273]$		Mg_2SiO_4	Wd/Rw	67
$P(\mathrm{GPa}) = 25.01 - 0.000765[T(^\circ\mathrm{C}) + 273]$[f]		Mg_2SiO_4	Rw/Bg + Per	68
Equation (1)		$En_{50}Cor_{50}$[g]	...	This study

[a] R.T.: room temperature; H.T.: high temperature.
[b] ZB, zinc blend structure; RS, rock salt structure; *Cmcm*, orthorhombic structure with space group *Cmcm*; Qz:, quartz; Cs, coesite; St, stishovite; Fa, fayalite; Ah: ahrensite; Fo, forsterite; Wd, wadsleyite; Rw, ringwoodite; Bg, bridgmanite; Per, periclase.
[c] Value recommended by Decker *et al.*[50]
[d] Average value of phase transition start and finish.
[e] Equation was fitted from the data of Katsura *et al.*[66] due to it was not provided in the original paper.
[f] The equation was fitted from Fig. 2(a) (1700–2040 K) of Chanyshev *et al.*,[68] due to it was not provided in the original paper.
[g] En: enstatite ($MgSiO_3$); Cor: corundum (Al_2O_3).

often complemented by high-temperature calibrations. Because of the different responses of assembly materials to temperature, it is possible that the room-temperature and high-temperature calibrations differ from each other.[32,34] In this overview, we critically examine historical datasets of widely used room-temperature as well as high-temperature pressure markers, utilizing a variety of well-established pressure markers, including the melting points of alkali halides (e.g., NaCl), phase transitions of selected metals and semiconductors (e.g., bismuth, barium, lead, tellurium, cadmium phosphide, zinc selenide, gallium arsenide, and gallium phosphide), and key mineral phase transitions (e.g., quartz–coesite in the SiO_2 system, and forsterite–wadsleyite and wadsleyite–ringwoodite in the Mg_2SiO_4 system). Additionally, the Al_2O_3 content in bridgmanite within the $MgSiO_3$–Al_2O_3 binary system is employed as a geochemically relevant pressure indicator under high-pressure conditions. We also propose a physically based fitting strategy for pressure calibration.

B. On pressure reference points

Despite extensive research since the pioneering work of Bridgman on the pressure-induced phase transition of solid materials,[53] discrepancies still exist in the literature regarding the precise phase transition pressures of certain pressure calibrants.[48–52] Advances in experimental techniques have led to more accurate and consistent determinations of pressure reference points in recent years. We have updated the common pressure reference points by thoroughly reviewing all available literature data and incorporating extensive validation as well as the latest research on phase transitions. This has resulted in a dataset of recommended phase transition pressures for calibrants, as listed in Table III. A comprehensive dataset with a compilation of historically reported phase transition pressures for those calibrants, including all available reference points and their sources, is provided in supplementary material A for future reference.

C. Identification of pressure reference points

The pressure calibrations described below span a temperature range from room temperature up to 1727 °C (2000 K), depending on the specific phase transition considered. Calibrations at room temperature are based on phase transitions in selected metals (Bi, Ba, Pb, and Te) and semiconductors (Cd_3P_2, ZnSe, GaAs, and GaP), which are accompanied by pronounced changes in their electrical properties. The four-electrode method is a widely adopted technique for accurate resistance measurement. It eliminates lead and contact resistance by separating the current-carrying and voltage-sensing paths.[69] This method is suitable for high-pressure applications requiring precise detection of phase transitions in metal calibrants. In this setup, two electrodes supply a constant current to the sample, while the other two measure the resulting voltage across the sample. The simpler two-probe method is used for resistivity measurement of semiconductors. Pressure-induced phase transitions in selected metals and semiconductors used for calibration are shown in Fig. 1. Electrical voltage U or resistance R was continuously monitored during compression, and the first derivatives dU/dP_{oil} or dR/dP_{oil} were calculated to accurately identify transition points. The compression rates for experiments on cubic presses and multi-anvil presses were 1 MPa/min and 0.3–1 bar/min, respectively.

Calibrations at high temperature were performed using the quench method, covering the temperature range between 905 °C (1178 K) and 1723 °C (2000 K), depending on the phase transition considered. Figure 2 shows representative examples of changes in Raman spectra used to determine the pressure at which a specific phase transition occurred when the SiO_2, Mg_2SiO_4, and Fe_2SiO_4 systems were used. The starting materials were amorphous SiO_2 powder, Mg_2SiO_4, and Fe_2SiO_4 powders, respectively.

The Al_2O_3 content in bridgmanite increases systematically with pressure when in equilibrium with corundum and can be used as a pressure calibrant.[70–72] To investigate this, two experiments were conducted to synthesize run products from an $En_{50}Cor_{50}$ starting composition (En = enstatite, $MgSiO_3$; Cor = corundum, Al_2O_3) at 1723 °C (2000 K), using the Kawai-type LPRU1500 multi-anvil press. The oil pressure was set to 200 and 250 bars for the perspective runs. The backscattered electron (BSE) images of the samples exhibit a fine-grained polycrystalline texture consisting of bridgmanite and corundum (Fig. 3). Al_2O_3 contents of bridgmanite can be obtained using electron microprobe analysis (EMPA).

The relationship between pressure and xAl_2O_3 (Al_2O_3 mole fraction of bridgmanite in $MgSiO_3$–Al_2O_3 binary end-member system) at 2000 K is shown by the best fit to all available experimental data, which yields the following equation:

$$P(\mathrm{GPa}) = (140.6 \pm 10.7) \cdot x\,Al_2O_3 + (9.7 \pm 2.1) \quad R^2 = 0.96. \quad (1)$$

D. Calibration curve fitting strategy

All components employed in LVP high-pressure experiments can be approximately treated as cellular solids or bulk solids, depending on their microstructure and mechanical features.[73–75] Under elevated pressures and temperatures, both plastic deformation and creep in such solids exhibit nonlinear viscoplastic stress–strain behavior,[76–79] which is primarily governed by microstructural and mechanical factors such as frictional resistance, strain hardening, grain boundary sliding, and constraints imposed by limited material compressibility.[73,80–84] An accurate description of this nonlinear behavior would require the construction of a viscoplastic constitutive model.[85–87] As an alternative, the Voce hardening law provides a simplified yet effective presentation that describes key features of classical viscoplastic behavior, particularly the observed nonlinear stress–strain response and the asymptotic approaching to a saturation stress.[76,88–91] In this study, we propose employing the modified Voce equation to describe the correlations between loading force and chamber pressure for assemblies with three or more pressure calibration points:

$$P(F) = P_0 + (P_{\max} - P_0)[1 - \exp(-F/F_c)], \quad (2)$$

where P is the chamber pressure (sample pressure), F is the external loading force, which is equivalent to and can be replaced with the cylinder oil pressure, the fit parameter P_0 corresponds to the initial chamber pressure at $F \to 0$ (i.e., $\lim_{F\to 0} P = P_0$), the fit parameter $P_{\max}$ characterizes the theoretical maximum attainable chamber pressure at $F \to \infty$ (i.e., $\lim_{F\to\infty} P = P_{\max}$), and the fit parameter F_c defines the characteristic loading force (or oil pressure) at which the chamber pressure transitions toward saturation. At $F = F_c$, the chamber pressure reaches 63.21% of its maximum value (that is

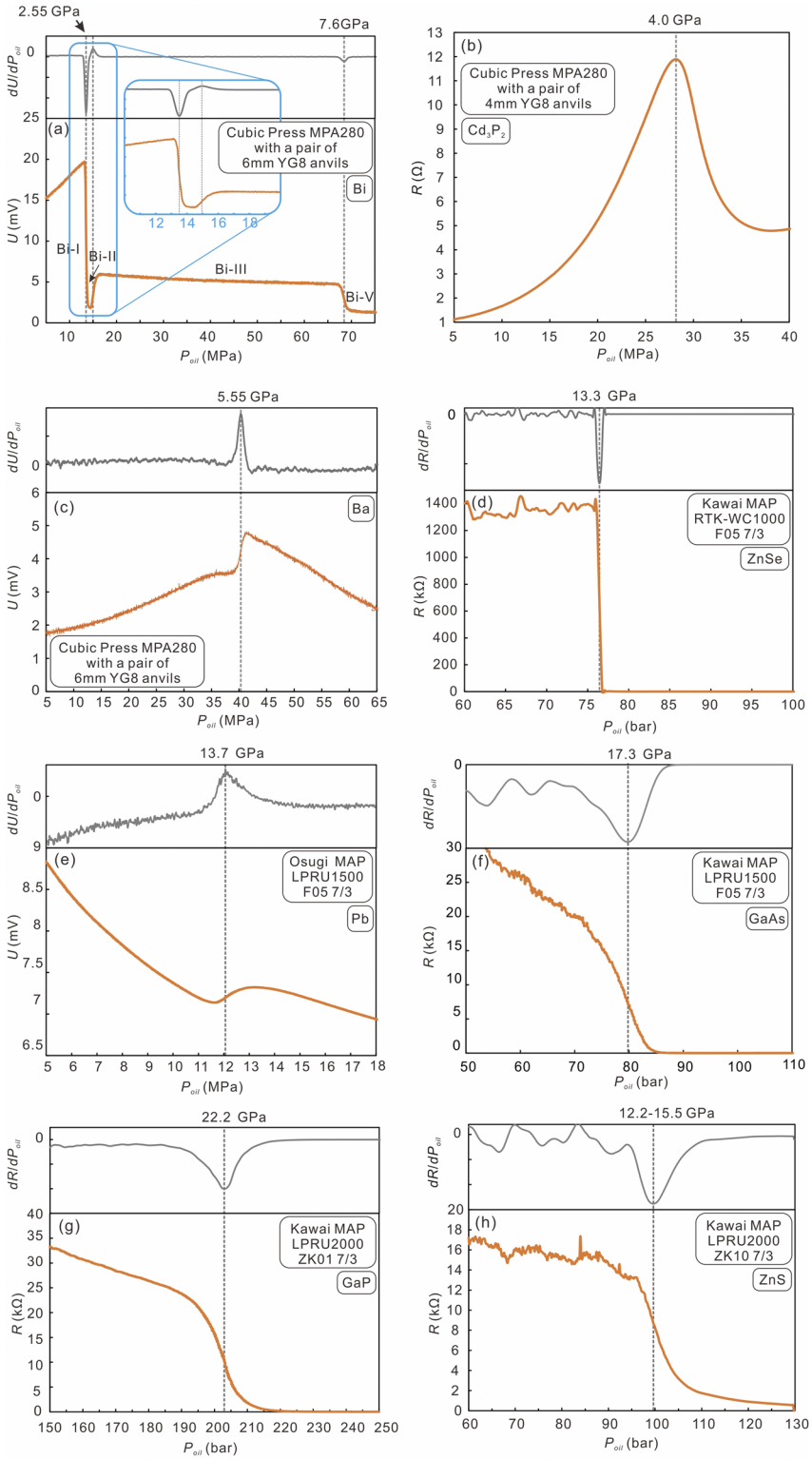

FIG. 1. Representative variations of voltage or resistance at room temperature during compression of (a) bismuth, (b) Cd_3P_2, (c) barium, (d) ZnSe, (e) lead, (f) GaAs, (g) GaP, and (h) ZnS. The phase transition pressure of ZnS remains controversial (see the discussion in Sec. V B). Note the derivatives dU/dP_{oil} and dR/dP_{oil} are also given at the tops of the corresponding panels.

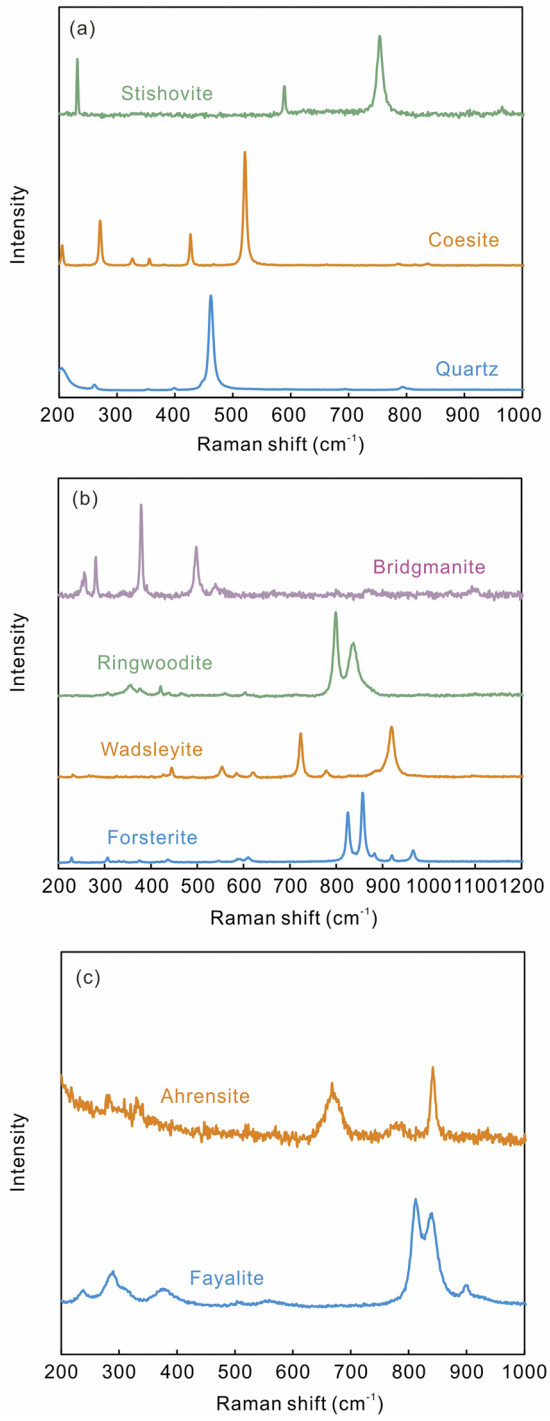

FIG. 2. Representative Raman spectra of (a) quartz, coesite, and stishovite from experiments using amorphous SiO_2 as a pressure calibrant, (b) forsterite, wadsleyite, ringwoodite, and bridgmanite from experiments using Mg_2SiO_4 powder as a pressure marker material, and (c) fayalite and ahrensite from experimental run products using Fe_2SiO_4 powder. Raman spectra were collected at HPSTAR using a WITec alpha300R Raman imaging microscope equipped with a 532 nm laser source, an 1800 grooves/mm grating, and exposure times of 30–50 s.

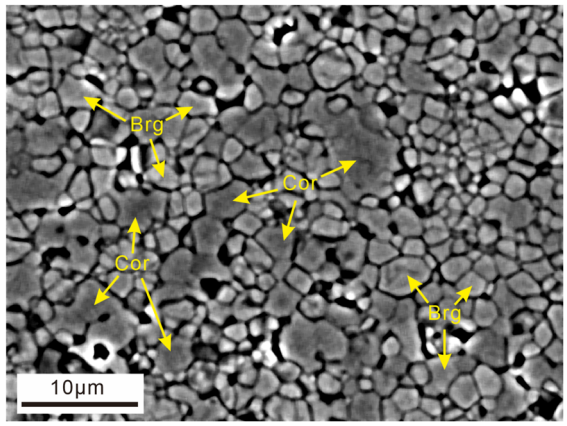

FIG. 3. Representative backscattered electron image of the run product for $En_{50}Cor_{50}$ synthesized at an oil pressure of 250 bars (≈7.07 MN) and a temperature of 2000 K for 3 h, using the Kawai-type LPRU1500 multi-anvil press.

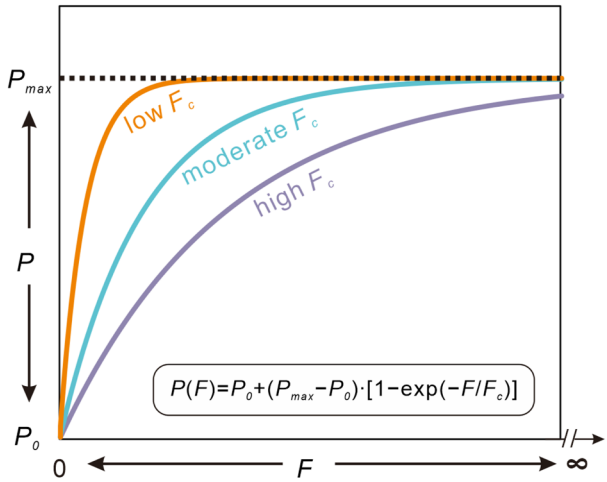

FIG. 4. Schematic of the nonlinear Voce relationship between loading force F and chamber pressure P.

$1 - 1/e$ of P_{max}). In this equation, the term $P_{max} - P_0$ describes the total increment in chamber pressure. A schematic of this description is shown in Fig. 4. Curve fitting can be performed using Origin or OriginPro software, and the details of the procedure are provided in supplementary material B. Because we perform both room-temperature and high-temperature calibrations in this work, we can assess the extent to which temperature affects the pressure calibration for each LVP and assembly.

We propose that pressure calibration curves should not be constrained to pass through the origin ($P_0 = 0$, $F = 0$), on the basis of the following considerations:

1. In the early stage of loading, the pressure medium may undergo significant volume reduction and deformation due

to the differing critical conditions for pore collapse vs plastic flow. This may cause deviations from classical viscoplastic behavior and introduce substantial errors in pressure estimation.
2. The efficiency of pressure transmission in an LVP is highly dependent on the geometry of the assembly, leading to variations in the initial pressure generation.
3. Mechanical friction resistance within the oil cylinder introduces nonlinear resistance, further compromising the uncertainty of pressure measurements at low pressures.

Furthermore, it should be noted that a negative best-fit P_0 value in Eq. (2) does not affect the precision within the calibrated pressure range, but caution is needed when extrapolating the curves.

IV. EXPERIMENTAL ASSEMBLIES AND CALIBRATION CURVES

A. Piston–cylinder press

A piston–cylinder press consists of a hydraulically driven piston that compresses a cylindrical sample assembly inside a pressure vessel. The pressure is applied through hydraulic cylinder, creating high-pressure conditions in the vessel, as in the two-platten Boyd–England design (Fig. 5). Such presses are suitable for research requiring high-temperature and high-pressure environments, with precise control of chamber temperatures via thermocouple measurements. The piston–cylinder press at HPSTAR can pressurize a sample from 0.4 to 3.14 GPa, covering conditions from the Earth's lower crust to the upper mantle. Two piston sizes are available: 3/4 in. (0.4–1.5 GPa) and 1/2 in. (1–3.14 GPa).

The structure and materials of the pressure-calibrated PC assembly are shown in Fig. 6. The outermost layer is made of talc, a soft, pressure-transmitting material that provides thermal insulation and helps distribute the applied pressure evenly. Pyrex glass surrounds the inner layers, offering further insulation of the core sample area. Thermocouple wires are inserted into the middle section of the assembly through the four-bore alumina (Al_2O_3) tube and connected at the interior end of the tube. A thin ceramic Al_2O_3 disk is put on the top of sample capsule to prevent reactions between sample capsule and the type-D (W_3Re_{25}) thermocouple at high temperature. Samples are heated to high temperatures using a graphite furnace. A steel cap surrounded by electrically insulating pyrophyllite is used to seal the assembly and apply pressure evenly to the sample from the top. The experiments are done using the piston-in technique, i.e., pressure is increased during heating, with the targeted pressure achieved as the targeted temperature is reached.

FIG. 5. Piston–cylinder press at HPSTAR.

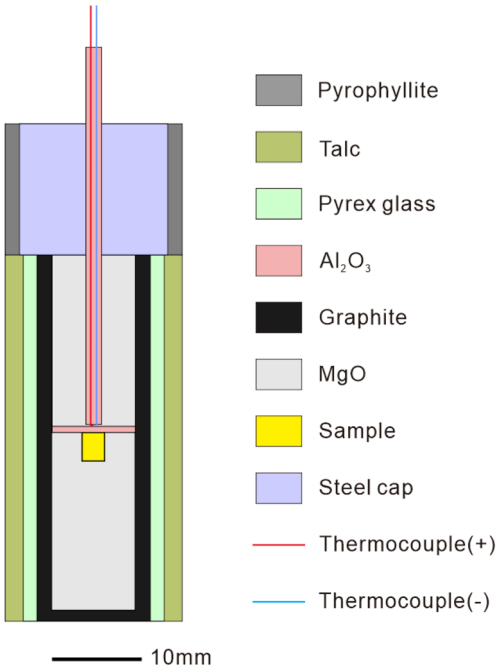

FIG. 6. The 3/4-in. (19 mm) assembly for the piston–cylinder press shown in a vertical section.

Pressure calibrations were performed for 3/4-in. (19 mm) and 1/2-in. (12.7 mm) diameter talc–Pyrex cell assemblies, using NaCl and SiO_2 as pressure standards in both, with the Bi I–II transition at room temperature assessed in addition for the 1/2-inch assembly. We use an Au sphere as a sinking marker in the NaCl melting experiments. Figure 7 illustrates the relationship between the oil pressure P_{oil} in psi and the sample pressure P_{sample} in GPa. For the 3/4-in. diameter assembly, the NaCl melting experiments were conducted at 940 and 1000 °C, corresponding to melting pressures of 0.7 and 1 GPa, respectively.[63] The pressure calibration used for the 1/2-in. diameter assembly focused on the melting of NaCl at 1000 °C and the quartz-to-coesite phase transition at 1100 °C.[47] The Bi I–II transition was studied at room temperature. Sample pressure and oil pressure show a linear relationship as is customary in piston–cylinder assemblies, and the calibration curves for the

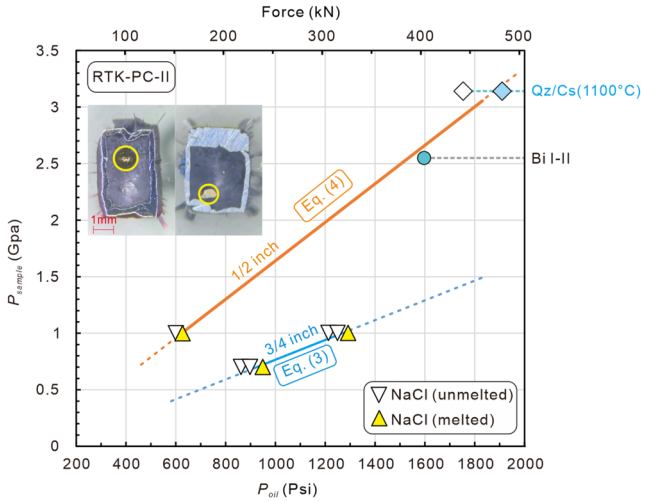

FIG. 7. Pressure calibration curves for piston–cylinder press. The blue and orange curves are for the 3/4-in. (19 mm) and 1/2-in. (12.7 mm) diameter assemblies. respectively. The dashed lines are extrapolations. The experimental temperature used to constrain the oil pressure for the quartz–coesite(Qz/Cs) phase transition is 1373 K (1100 °C). The photographs at the upper left show cross-sections of the run products from NaCl melting experiments, with yellow circles indicating the positions of gold spheres.

3/4-in. (19 mm) and 1/2-in. (12.7 mm) diameter assemblies are defined as

$$P_{sample} = 8.746 \times 10^{-4} P_{oil} - 1.090 \times 10^{-1}, \quad (3)$$

$$P_{sample} = 1.703 \times 10^{-3} P_{oil} - 6.256 \times 10^{-2}, \quad (4)$$

respectively (with P_{sample} in GPa and P_{oil} in psi). Temperature appears to have no significant effect on the calibration curve for the 1/2-in. assembly (Fig. 7).

B. Cubic press

The four cubic presses at HPSTAR comprise one MPA280 with a force up to 6 × 6 MN; two GY420 with a force up to 6 × 14 MN, and one GY560 with a force up to 6 × 27 MN. Each press features six identical jacks attached to a frame, and their movements are perpendicular to one another. These jacks are driven by a computer-controlled hydraulic system. A linear sensor system surrounding the central cubic space precisely monitors the relative positions of the six anvils (Fig. 8). The anvil top edge lengths are 18 mm (MPA280), 27.5 mm (both GY420 devices), and 42.5 mm (GY560).

The primary components of the assembly include a cubic block of natural pyrophyllite briquettes (produced from the Mentougou region, China, with an edge length of 28 mm for the MPA280,

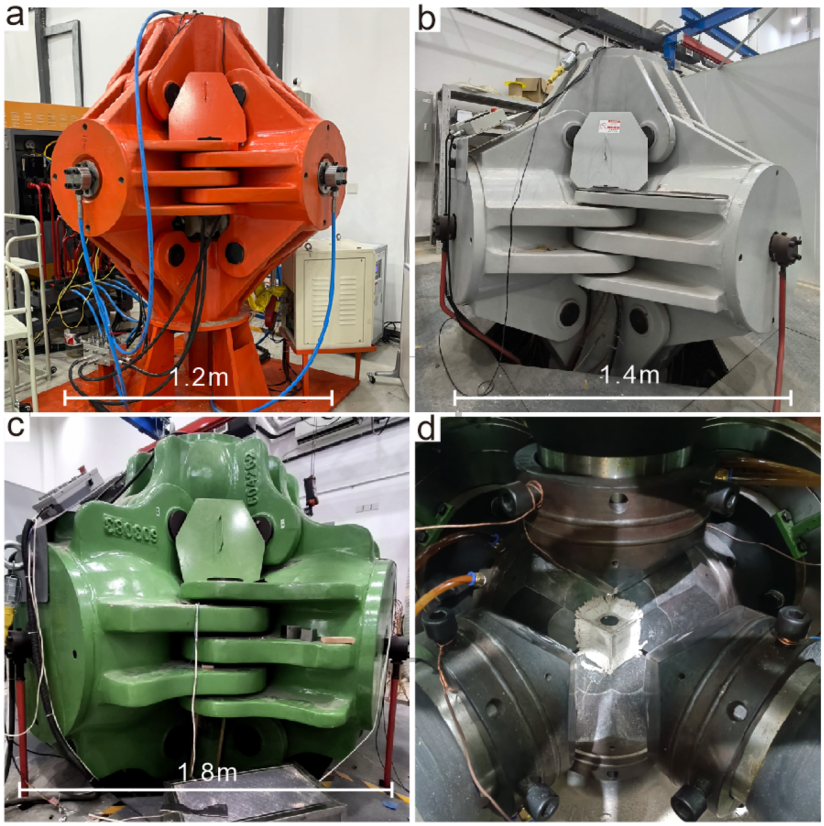

FIG. 8. (a)–(c) Photographs of MPA280, GY420, and GY560 cubic presses, respectively. (d) Photograph of six tungsten carbide (WC) anvils and a compressed cubic assembly inside the GY560 cubic press.

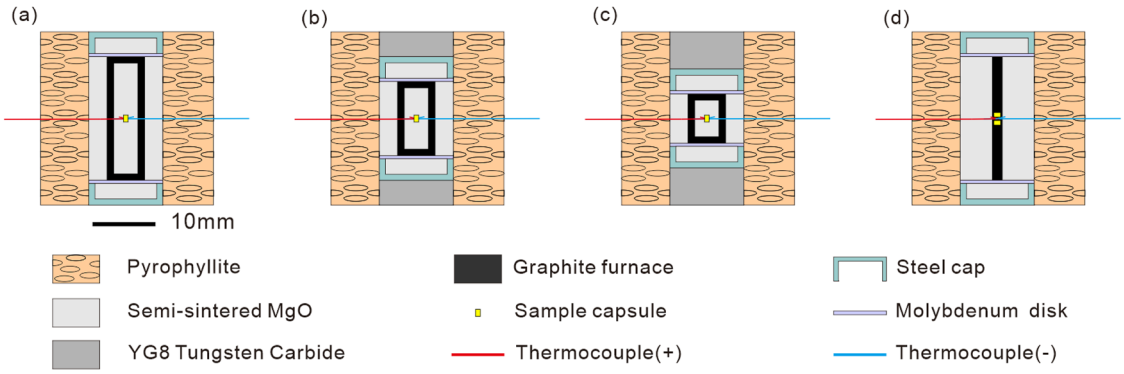

FIG. 9. Overview of experimental assembly designs for MPA280 cubic presses. (a) Traditional assembly; (b) traditional assembly with a pair of 4 mm thick YG8 anvils (HRA ≈88); (c) traditional assembly with a pair of 6 mm thick YG8 anvils; (d) rapid cooling assembly. Modified after Wu *et al.*[92]

38.5 mm for the GY420, and 52.5 mm for the GY560), sintered MgO sleeves, steel cap, molybdenum disk, and graphite furnace (Fig. 9). The natural pyrophyllite was stored in a furnace at 120 °C until use.

Four widely used types of assembly blocks are shown in Fig. 9. The traditional assembly graphite furnace is tube-shaped with two lids at the top and bottom. An MgO rod is inserted into the tubular graphite furnace to support the sample capsule and help retain heat [Fig. 9(a)]. This design can achieve pressures up to ~5.55 GPa. If higher chamber pressures are required, a pair of secondary YG8 (Rockwell hardness HRA ≈88) tungsten carbide anvils can be added at the top and bottom of the block [Figs. 9(b) and 9(c)]. A recently developed rapid cooling assembly is shown in Fig. 9(d). Instead of a tubular graphite furnace, a slim graphite rod is placed vertically in the center, and sample capsules are inserted into this rod, which can significantly increase the cooling rate.[92] If it is desired to attain a higher chamber pressure with a high cooling rate, secondary tungsten carbide anvils can also be used in combination with this setup.

In the traditional assembly [Figs. 9(a)–9(c)], temperatures are measured using tungsten–rhenium thermocouple wire pairs that are radially inserted and wrapped around the sample capsule, with the junction positioned at the center of the assembly without insulation. For the rapid cooling assembly [Fig. 9(d)], the thermocouple wires are wrapped at the center of the graphite rod, with the sample capsules inserted adjacent to the thermocouple junction.

The above experimental setup can generate pressures up to 5.55 and 7.6 GPa in the MPA280 cubic press (Fig. 10) by using low-pressure and high-pressure assemblies with different thicknesses of secondary anvils, respectively. They are calibrated by the room-temperature Bi I–II phase transition, Cd_3P_2 I–II phase transition, Ba I–II phase transition, Bi III–V phase transition, and the high-temperature fayalite–ahrensite phase transition at 1473 K (1200 °C). The relationships between P_{oil} and P_{sample} are derived from best fits of the room-temperature calibration data to the Voce equation [Eq. (2), with P_{sample} in GPa and P_{oil} in MPa]:

$$P_{sample} = -0.418 + (7.100 + 0.418)[1 - \exp(-P_{oil}/46.803)], \quad (5)$$

$$P_{sample} = -1.008 + (7.258 + 1.008)[1 - \exp(-P_{oil}/30.376)], \quad (6)$$

$$P_{sample} = 0.489 + (11.283 - 0.489)[1 - \exp(-P_{oil}/63.703)]. \quad (7)$$

Figure 10 shows that the room-temperature calibration curve agrees very well with the location of the 1200 °C fayalite–ahrensite transition, suggesting that the temperature effect on the pressure calibration curve for this setup is insignificant.

Pressures as high as 5.55 GPa can be generated on the GY420 cubic press (Fig. 11), depending on whether a secondary anvil is used in the assembly block (Fig. 9). Using observations of the room-temperature Bi I–II, Cd_3P_2 I–II, and Ba I–II phase transitions, the quartz–coesite transition at 1273 K (1000 °C), and

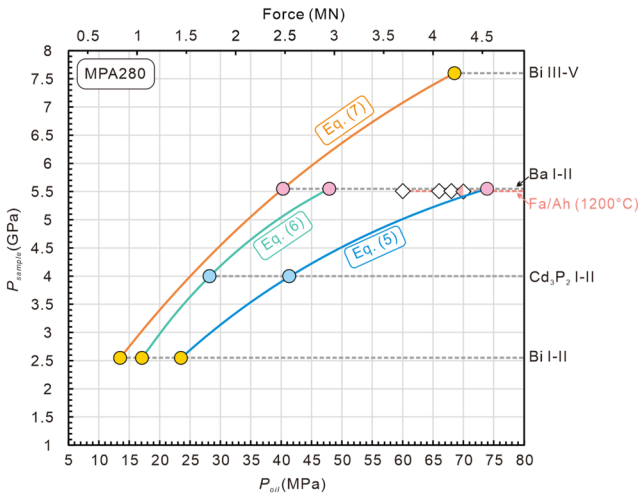

FIG. 10. Pressure calibration curves for the MPA280 cubic press. The blue curve is calibrated using the low-pressure assembly [Figs. 9(a) and 9(d)], the green and orange curves are for high-pressure assemblies [Figs. 9(b) and 9(c)] with a pair of 4 and 6 mm secondary YG8 anvils, respectively. The anvil grade is ZK20A, the anvil top edge length is 18 mm, and the dimensions of the pressure medium are 28 × 28 × 28 mm^3. Fa, fayalite; Ah, ahrensite; open diamonds, Fa only; half-colored diamond, Fa and Ah coexisting.

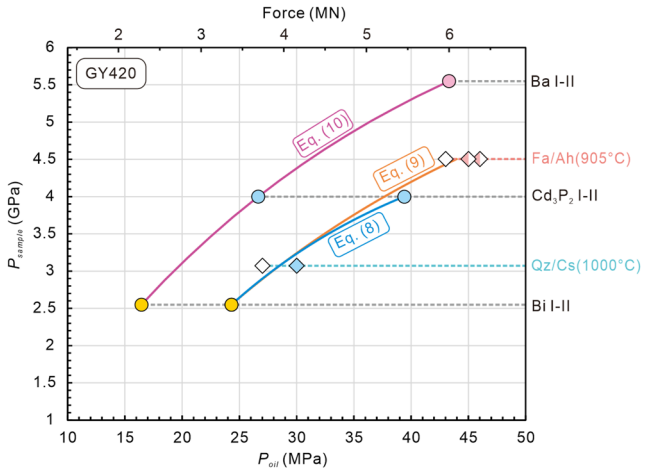

FIG. 11. Pressure calibration curve for the GY420 cubic press. The blue curve is calibrated using room-temperature Cd_3P_2 phase transition data, while the orange curve is calibrated using high-temperature fayalite–ahrensite phase transition data with the traditional assembly [Fig. 9(a)]. The purple curve is calibrated for the high-pressure assembly with 5 mm thick YG8 secondary anvils. The blue solid diamond indicates the presence of coesite, and half-filled diamonds indicate the coexistence of fayalite and ahrensite phases. The anvil grade is JN8, the anvil top edge length is 27.5 mm, and the dimensions of the pressure medium are 38.5 × 38.5 × 38.5 mm^3.

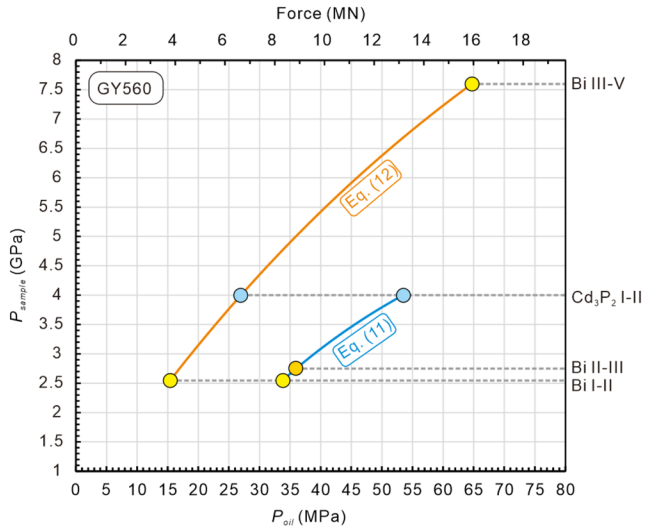

FIG. 12. Pressure calibration curves for the GY560 cubic press. The blue and orange curves are for the traditional assembly [Fig. 9(a)] and the high-pressure assembly with 14 mm thick YG8 secondary anvils [Fig. 9(d)], respectively. The anvil grade is GF35H, the anvil top edge length is 42 mm, and the dimensions of the pressure medium are 52.5 × 52.5 × 52.5 mm^3.

the fayalite–ahrensite transition at 1178 K (905 °C), the pressure calibration curves are given by

$$P_{sample} = -4.217 + (5.215 + 4.217)[1 - \exp(-P_{oil}/19.227)], \quad (8)$$

$$P_{sample} = -2.180 + (6.906 + 2.180)[1 - \exp(-P_{oil}/33.051)], \quad (9)$$

$$P_{sample} = -1.021 + (7.803 + 1.021)[1 - \exp(-P_{oil}/31.713)] \quad (10)$$

(with P_{sample} in GPa and P_{oil} in MPa). The high-temperature calibration curve [Eq. (9)] lies slightly above the room-temperature curve [Eq. (8)], but this small effect is only seen at high pressure, consistent with previous comparisons between low-temperature and high-temperature calibration curves.[32,34]

The GY560 cubic press has a similar pressure capacity as the GY420 device (Fig. 12). Based on room-temperature phase transitions of Bi and Cd_3P_2, the pressure calibration curves are given by

$$P_{sample} = -2.329 + (6.339 + 2.329)[1 - \exp(-P_{oil}/40.844)], \quad (11)$$

$$P_{sample} = 0.297 + (14.309 - 0.297)[1 - \exp(-P_{oil}/87.850)] \quad (12)$$

(with P_{sample} in GPa and P_{oil} in MPa). It should be noted that although the Bi II–III transition was used in fitting Eq. (11), it is not recommended as a calibration reference point, owing to its proximity to the Bi I–II transition, which probably introduces significant distortion in the fitting curve. Here, we adopt the newly reported Bi II–III phase transition pressure of 2.75 GPa.[93]

C. Multi-anvil press

HPSTAR Beijing has three Kawai-type multi-anvil presses (KMAPs) with a split-sphere-type guide block [RTK-WC1000, LPRU1500, and LPRU2000; Figs. 13(a)–13(c)] and one with an Osugi-type (DIA-type) guide block [LPRU1500; Fig. 13(d)]. The maximum loads of RTK-WC1000, LPRU1500, and LPRU2000 are 1000 ton-force (≈10 MN), 1500 ton-force (≈15 MN), and 2000 ton-force (≈20 MN), respectively.

Depending on the choice of assembly, anvil truncated edge length (TEL), and anvil material, the pressures that can be routinely generated by these multi-anvil presses range from 2.55 to 30.6 (±2.6) GPa, with temperatures exceeding 2300 °C. This is equivalent to the pressure–temperature conditions from the top of Earth's upper mantle to the top of the lower mantle.

Cross-sections of the cell assemblies for the multi-anvil presses are shown in Fig. 14. The primary components of the assemblies include an octahedron of magnesium oxide (MgO) doped with 5 wt. % chromium oxide (Cr_2O_3). Rhenium foil or lanthanum chromite ($LaCrO_3$) is used as a furnace, surrounded by thermal insulation material, normally a zirconium oxide (ZrO_2) and $LaCrO_3$ tube. Sample capsules are placed at the center of a MgO sleeve. The widths of the pyrophyllite gaskets used with these assemblies are 4.5, 3, and 2 mm for the 14/8, 7/3, and 5.7/1.5 assemblies, respectively.

Depending on the specific experimental requirements, two types of thermocouple arrangements are employed. In the first configuration applied to 14 mm edge length octahedra, the thermocouple passes through a four-bore Al_2O_3 tube and is bent to fit into a shallow groove at the top of the octahedron [Fig. 14(a)]. In the second configuration, the thermocouple wires are inserted horizontally, passing through the middle of the rhenium or $LaCrO_3$ heater [Figs. 14(b) and 14(c)]. The latter is usually employed in the smallest

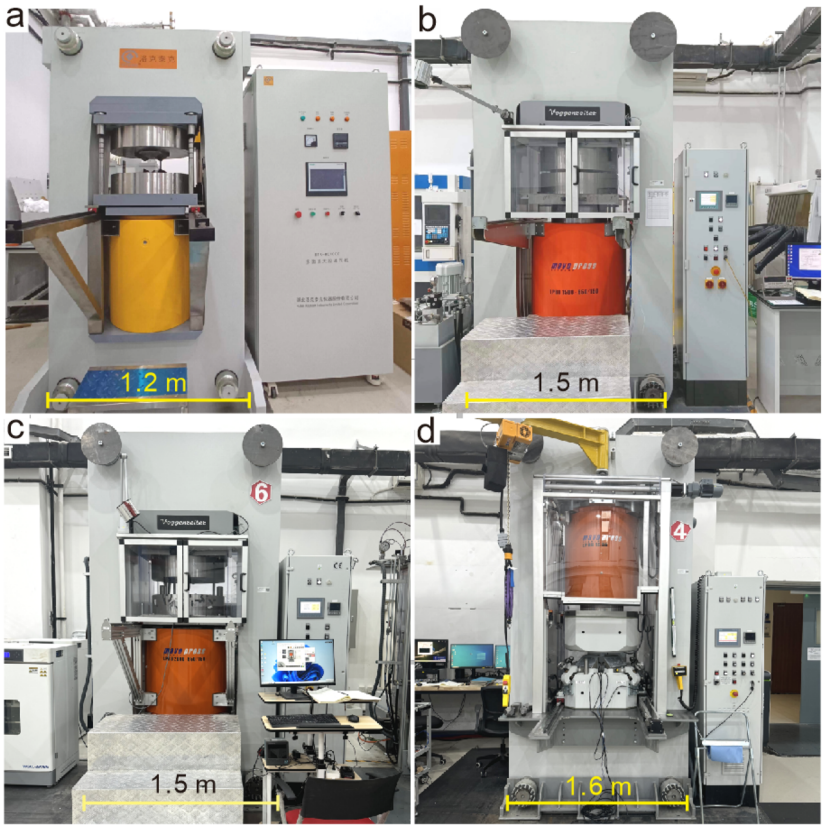

FIG. 13. Photographs of the multi-anvil presses at HPSTAR: (a) Kawai-type model RTK-WC1000; (b) Kawai-type model LPRU1500; (c) Kawai-type model LPRU2000; (d) Osugi-type model LPRU1500.

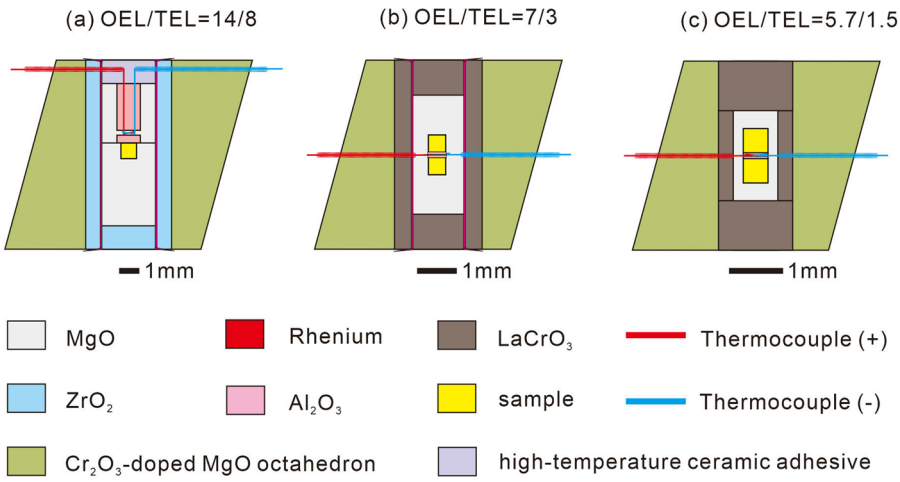

FIG. 14. Cross-sections of cell assemblies used in multi-anvil presses: (a) rhenium heater assembly for 14 mm edge length octahedron; (b) rhenium heater assembly with $LaCrO_3$ thermal insulator for 7 mm edge length octahedron; (c) $LaCrO_3$ heater assembly for 5.7 mm edge length octahedron. The pyrophyllite gaskets used in these assemblies are trapezoidal plates. Detailed size parameters are shown in Table IV.

assemblies with an octahedron edge length (OEL) of 7 or 5.7 mm. Sample capsules can be placed on one side or both sides of the thermocouple junction, depending on experimental requirements.

1. Kawai-type multi-anvil press with a split-sphere-type guide block

The pressure calibration curves for the Kawai-type RTK-WC1000 press are based on phase transitions of Bi, GaAs, GaP, Te, SiO_2, and Mg_2SiO_4, and are shown in Fig. 15. The blue, orange, purple, and green pressure curves are for Cr_2O_3-doped MgO octahedra with octahedral edge length/truncated edge length ratios (OEL/TEL) of 14/8 (using ZK10 anvils), 7/3 (using ZK01 anvils), 7/3 (using F05 anvils), and 5.7/1.5 (using ZK01 anvils), respectively. The gray curve for a 14/8 assembly labeled "Eq. (13)" is calibrated with CoO-doped MgO octahedra. The calibration curves are given by

TABLE IV. Size parameters of trapezoidal pyrophyllite gasket plates.

Assembly (OEL/TEL)[a]	Gasket	Thickness (mm)	Width (mm)	Front length (mm)	Back length (mm)
14/8	Long	2.83	4.5	14	23
	Short	2.83	4.5	10	19
7/3	Long	1.88	3	7	13
	Short	1.88	3	4.33	10.33
5.7/1.5	Long	1.98	2	5.7	9.7
	Short	1.98	2	2.9	6.9

[a]OEL, octahedron edge length; TEL, truncated edge length.

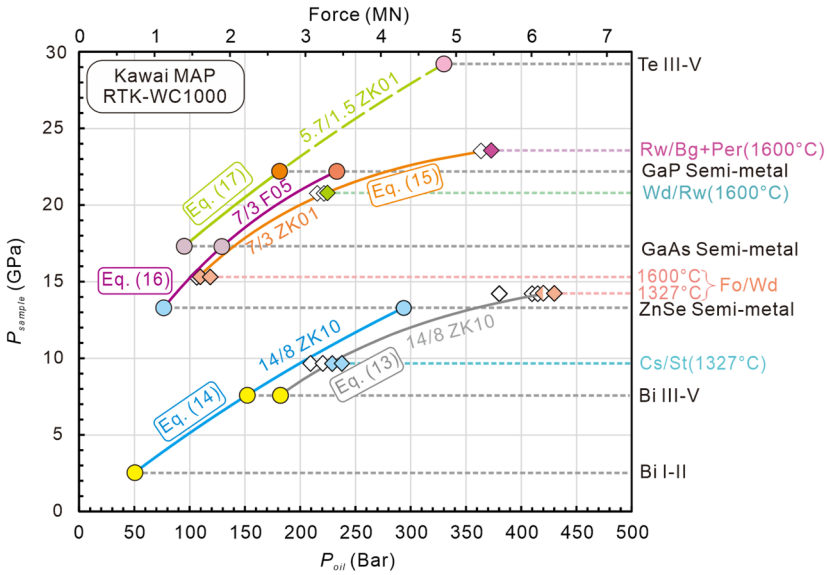

FIG. 15. Pressure calibration curves for the Kawai-type RTK-WC1000 multi-anvil press. Different grades of anvils are used for different TEL setups. Owing to the limited quality of the Te phase transition data, the upper part of Eq. (17) curve is shown as a dashed line. Cs, coesite; St, stishovite; Fo, forsterite; Wd, wadsleyite; Rw, ringwoodite; Bg, bridgmanite; Per, periclase. The half-filled diamond indicates coexistence of Fo and Wd phases, and the solid diamonds indicate that only high-pressure phases are present.

$$P_{sample} = -9.811 + (16.241 + 9.811)[1 - \exp(-P_{oil}/164.916)], \quad (13)$$

$$P_{sample} = -0.292 + (33.993 + 0.292)[1 - \exp(-P_{oil}/581.277)], \quad (14)$$

$$P_{sample} = 4.052 + (25.095 - 4.052)[1 - \exp(-P_{oil}/140.729)], \quad (15)$$

$$P_{sample} = 4.678 + (27.723 - 4.678)[1 - \exp(-P_{oil}/163.180)], \quad (16)$$

$$P_{sample} = 11.102 + (55.992 - 11.102)[1 - \exp(-P_{oil}/639.402)] \quad (17)$$

(with P_{sample} in GPa and P_{oil} in bars). Because the room-temperature and high-temperature experiments in Fig. 15 were performed with different octahedron materials, it is not possible to independently assess the effect of temperature on the location of the calibration curves.

The pressure calibration curves for the Kawai-type LPRU1500 press are shown in Fig. 16 and cover the phase transitions of Bi, Pb, GaAs, GaP, Mg_2SiO_4, and Al_2O_3 solubility in bridgmanite. The blue curve corresponds to an OEL/TEL ratio of 14/8 at room temperature. To account for the large uncertainty in the bridgmanite-derived pressure data, the orange and green curves in Fig. 16 show calibrations with and without the bridgmanite-based high-temperature data points, respectively. The corresponding equations are

$$P_{sample} = -0.126 + (39.633 + 0.126)[1 - \exp(-P_{oil}/430.590)], \quad (18)$$

$$P_{sample} = -11.512 + (23.767 + 11.512)[1 - \exp(-P_{oil}/47.846)], \quad (19)$$

$$P_{sample} = (1.71 \pm 4.30) + (33.98 \pm 5.92) \times \{1 - \exp[-P_{oil}/(134.42 \pm 50.42)]\} \quad (20)$$

(with P_{sample} in GPa and P_{oil} in bars). The high-temperature forsterite–wadsleyite phase transition data points for the 14/8 assembly are located to the right of the room-temperature calibration curve (Fig. 16). However, as was the case in the calibrations shown in Fig. 15, the high-temperature 14/8 experiments were performed using a different octahedron composition to that used in the

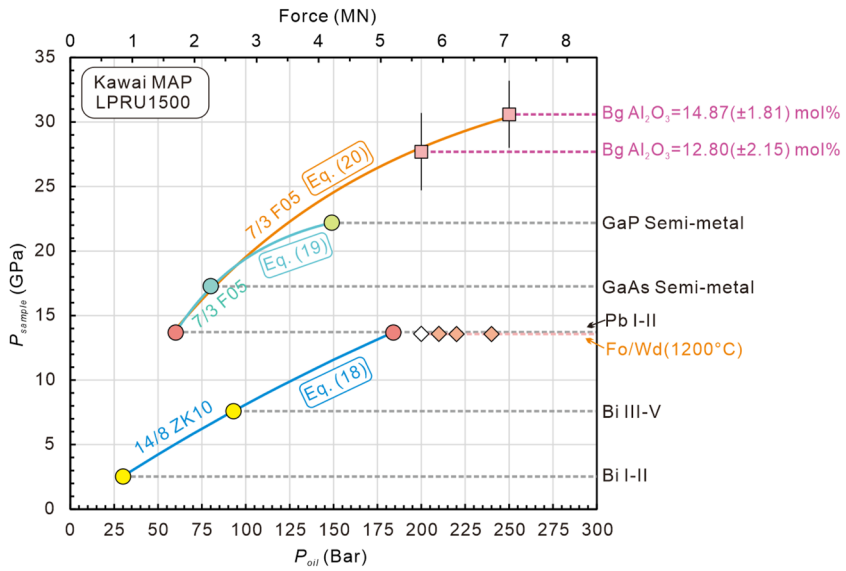

FIG. 16. Pressure calibration curves for the Kawai-type LPRU1500 press. Bridgmanite (Bg) contains 12.80 ± 2.15 mol. % Al_2O_3 at 200 bars, and 14.87 ± 1.81 mol. % Al_2O_3 at 250 bars in the $MgSiO_3$–Al_2O_3 binary end-member system. Equation (1) is used here to calculate the sample pressure: P(GPa) = (140.6 ± 10.7) · xAl_2O_3 + (9.7 ± 2.1). The GaP data are excluded in Eq. (20), owing to the temperature effect at higher pressure. The phase transition of forsterite (Fo)–wadsleyite (Wd) was calibrated using a CoO-doped MgO octahedron and is excluded from curve fitting.

low-temperature experiments. It is therefore not possible to ascribe this apparent shift in calibration curve to temperature. The high-temperature calibration curve for the 7/3 assembly [Eq. (20)] lies slightly above the room-temperature curve [Eq. (19)]. Again, this effect is only seen at high pressure, consistent with previous comparisons between low-temperature and high-temperature calibration curves.[32,34]

The pressure calibration curves for the Kawai-type LPRU2000 press are constructed using the phase transitions of Bi, Pb, ZnSe, ZnS, GaAs, GaP, forsterite–wadsleyite, and wadsleyite–ringwoodite phase transitions (Fig. 17) and are given by

$$P_{sample} = -0.549 + (32.606 + 0.549)[1 - \exp(-P_{oil}/295.520)], \quad (21)$$

$$P_{sample} = -10.401 + (23.602 + 10.401)[1 - \exp(-P_{oil}/75.881)], \quad (22)$$

$$P_{sample} = 0.982 + (25.906 - 0.982)[1 - \exp(-P_{oil}/71.884)], \quad (23)$$

$$P_{sample} = 9.674 + (40.199 - 9.674)[1 - \exp(-P_{oil}/226.225)] \quad (24)$$

(with P_{sample} in GPa and P_{oil} in bars). There are insufficient data points to provide calibration curves for the 7/3 assembly with ZK01

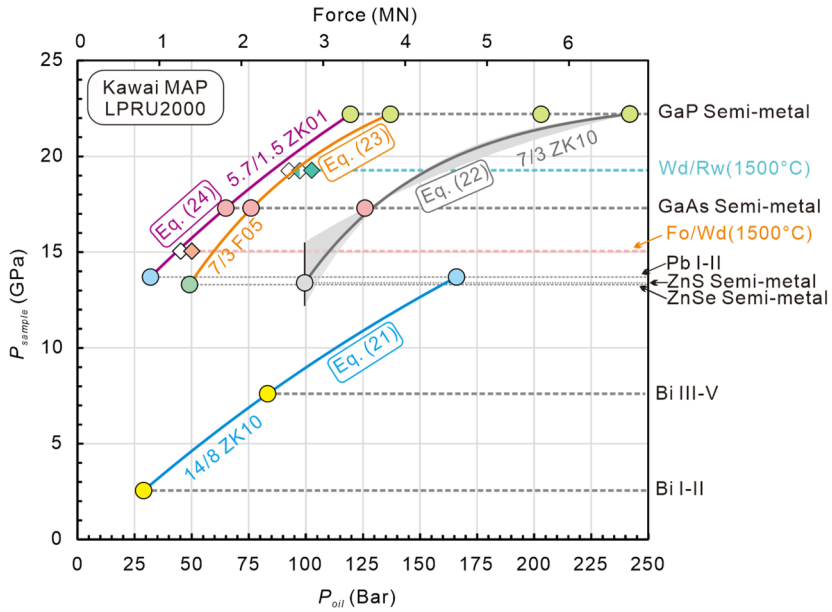

FIG. 17. Pressure calibration curves for the Kawai-type LPRU2000 press. Data for the forsterite–wadsleyite and wadsleyite–ringwoodite phase transitions and a GaP phase transition, which were obtained using ZK01 anvils with an OEL/TEL ratio of 7/3, were excluded from the fitting owing to uncertainties regarding the temperature effect at high pressure. The gray band in Eq. (22) calibration curve indicates the uncertainty propagated from the uncertain phase transition pressure of ZnS, which ranges from 12.2 to 15.5 GPa, while the solid gray circle denotes the newest value of 13.4 GPa reported by Ono and Kikegawa[94] (see the discussion in Sec. V B).

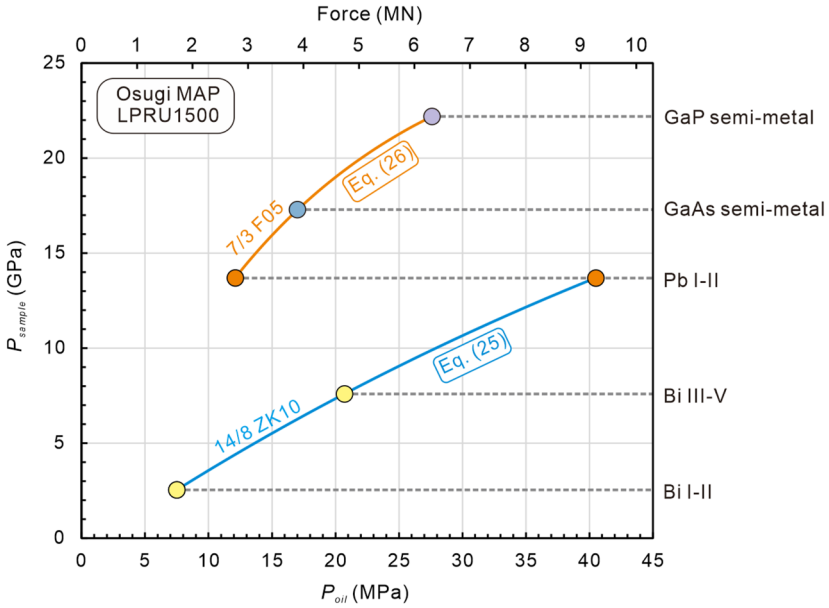

FIG. 18. Pressure calibration curves for Osugi-type LPRU1500 press.

cubes, but for completeness we report the transition points that we obtained (one at room temperature and two at high temperature).

2. Kawai-type multi-anvil press with an Osugi (DIA)-type guide block

The pressure calibration curve for the Osugi-type LPRU1500 press is based on observations of the Bi, Pb, GaAs, and GaP phase transitions (Fig. 18). Two curves are determined by an OEL/TEL ratio of 14/8 and 7/3 with grade ZK10 and F05 anvils, respectively, and are given by

$$P_{sample} = -0.731 + (34.269 + 0.731)[1 - \exp(-P_{oil}/76.190)], \quad (25)$$

$$P_{sample} = -1.234 + (27.770 + 1.234)[1 - \exp(-P_{oil}/16.727)] \quad (26)$$

(with P_{sample} in GPa and P_{oil} in MPa).

V. DISCUSSION

A. Comparison between different devices

Directly comparing the pressure generation efficiency among different cubic presses is challenging, owing to variations in cylinder bore diameters, anvil top edge lengths, and cell assembly configurations. Instead of performing complex mechanical calculations, here we propose the cylinder bore area to anvil top area (CBA/ATA) ratio as an empirical parameter for evaluating pressure generation efficiency for cell assemblies without secondary anvils, which can be used to predict the attainable sample pressure during press design and optimization. The CBA/ATA ratio can be calculated by the following equation:

$$\mathrm{CBA/ATA} = \frac{\pi(D/2)^2}{L^2}, \quad (27)$$

where D is the cylinder bore diameter in m and L is the anvil top edge length in m. The pressure generation efficiency is inversely correlated with the CBA/ATA ratio, which means that a cubic press with lower CBA/ATA ratio requires a higher oil pressure to achieve the same sample pressure (Fig. 19), yielding the following relationships at 2.55 and 4.0 GPa, respectively:

$$P_{oil}(\mathrm{MPa}) = (62.2 \pm 1.9) - (0.205 \pm 0.011)(\mathrm{CBA}/ATA), R^2 = 0.99, \quad (28)$$

$$P_{oil}(\mathrm{MPa}) = (91 \pm 12) - (0.27 \pm 0.07)(\mathrm{CBA}/ATA), R^2 = 0.88. \quad (29)$$

For Kawai-type and Osugi-type multi-anvil presses, in principle, when the anvil material, truncation length, and assembly configuration are identical, different multi-anvil presses should yield the same loading force vs sample pressure curves. However, in practice, differences in mechanical rigidity, frame deformation, alignment precision, component wear, and friction between moving components, as well as error propagation during unit conversion and calculation often result in distinct loading force vs sample pressure relationships among different multi-anvil presses.

Significant differences are observed between Kawai (split-sphere)-type and Osugi (DIA)-type multi-anvil presses. The split-sphere design generally exhibits a steeper loading force vs sample pressure curve. Notably, the Kawai-type MAP RTK-WC1000, LPRU1500 and LPRU2000 presses display similar slopes of loading force vs sample pressure relationships, demonstrating the reproducibility attainable with a unified design and manufacturing process [Fig. 20(a)]. The RTK-WC1000 press achieves slightly higher sample pressures for a given applied force, reflecting differences in press design and mechanical efficiency [Figs. 20(a)–20(c)]. By comparison, the Osugi (DIA)-type press, with its substantially different geometry and compression style, needs more force than the split-sphere type to obtain an identical sample pressure, as reflected

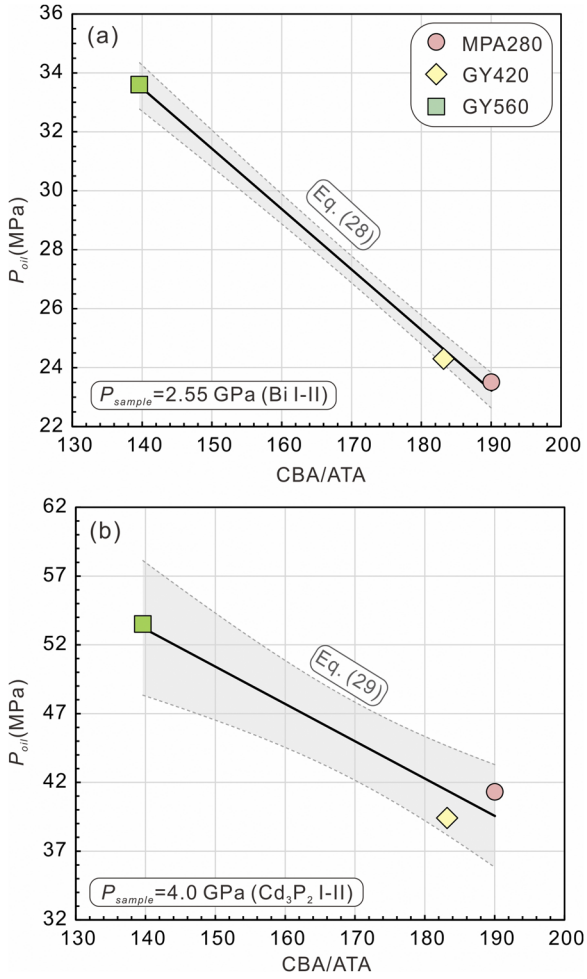

FIG. 19. Correlations of cylinder bore area to anvil top area (CBA/ATA) ratio with oil pressure at sample pressures of (a) 2.55 and (b) 4.0 GPa for cubic presses. Shaded regions indicate the $\pm 1\sigma$ confidence interval.

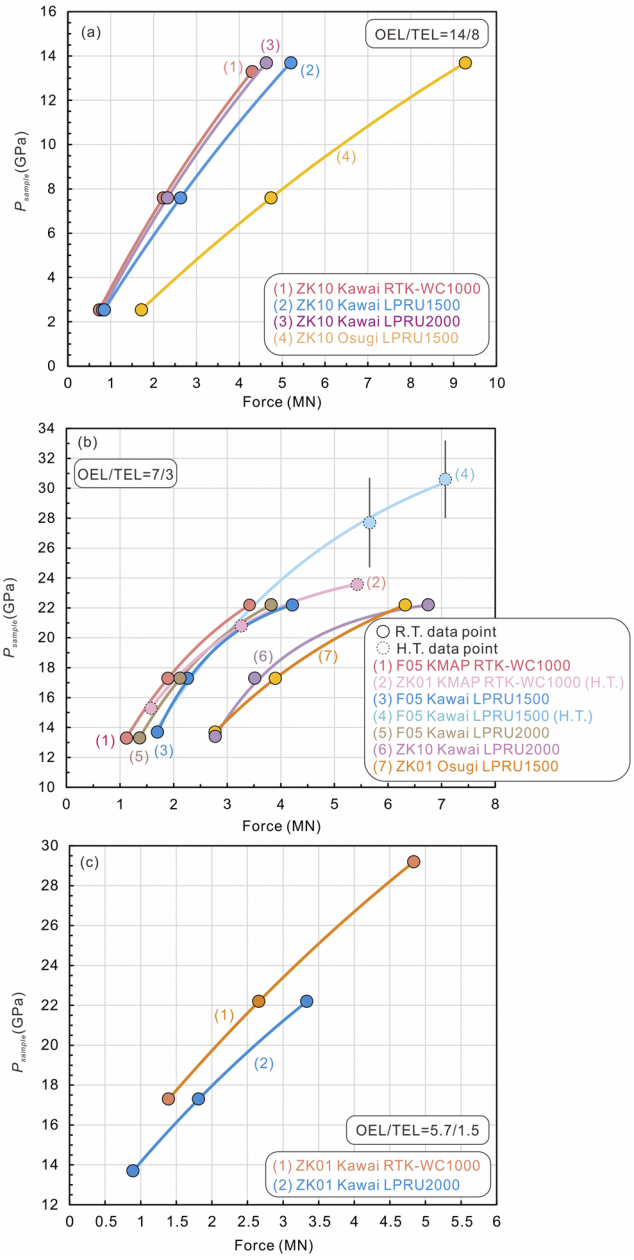

FIG. 20. Voce-fitted curves between loading force and sample pressure.

by its considerably lower slope of loading force vs sample pressure curves [Figs. 20(a) and 20(b)]. From a geometric perspective, to reach the same sample pressure, an Osugi-type press must supply $\sqrt{3}$ (≈1.732) times more loading force than a split-sphere-type press.[51,52] However, our calibration data indicate that for experimental setups using the 14/8 and 7/3 assemblies, the Osugi-type press requires ~1.5–2.3 times the loading force of the Kawai-type press to achieve the same sample pressure (Fig. 20). All the above factors and observations complicate direct comparisons between presses. This systematic variability reflects the impact of press design and force transmission mechanisms on calibration curves, and highlights the necessity of independent pressure calibration for each multi-anvil press.

B. Unsuitable and imperfect pressure calibrants

In previous pressure calibration studies, the room-temperature semiconductor-to-metal transition of ZnS and the room-temperature phase transitions of ZnTe have also been utilized, in addition to the calibrants listed in Table III. However, previously reported transition pressures for ZnS show extremely large variations from 12.2 to 25 GPa.[94–96] In addition to the significant overestimation of transition pressure in early studies caused by the imperfect pressure scales before the ruby fluorescence pressure scale was established and differences in pressure determination methods, this wide range can be primarily attributed to two factors: (i) the pressure-induced semiconductor-to-metal transition in ZnS is highly sensitive to grain size, and uncontrolled or variable particle sizes can introduce substantial errors in pressure determination[97,98]

and (ii) significant hysteresis is associated with the phase transition of ZnS at temperatures below 500 K.[95] These issues together indicate that ZnS may not suitable as a pressure calibrant at room temperature. The phase transition pressure range of 12.2–15.5 GPa used in Eq. (22) (Fig. 17) encompasses all newer values reported since the 1990s (see supplementary material A).

Previous calibration studies usually interpreted a resistance change observed around 6.6 GPa in ZnTe as a structural phase transition from phase I to phase II.[31,39,42,99–101] Actually, no transition has been detected in this pressure range on the basis of X-ray diffraction (XRD) or Raman spectroscopy methods. The phase transitions of ZnTe-I to ZnTe-II (zinc blende-type to cinnabar-type structure) and ZnTe-II to ZnTe-III (cinnabar-type to *Cmcm*-type phase) occur over broad pressure ranges of 9–and 10.7–13 GPa, respectively.[102] This oft-cited resistance anomaly is related to a deep-to-shallow transition of acceptor levels, rather than a structural phase transition.[103] Although ZnTe exhibits a notable U-shaped resistivity change around 5–7 GPa, this transition does not show a sharp turning point,[104] and a similar pattern of variation of resistivity was not observed in measurements by Cui *et al.*[103] In addition, the resistance changes occasionally significantly lag behind or precede the structural phase transitions for both ZnTe-I to ZnTe-II and ZnTe-II to ZnTe-III.[105] Therefore, ZnTe is of limited utility as a pressure calibrant. Instead, the zinc blende to rock salt structural transition of ZnSe is recommended for pressure calibration at 13.3 GPa, owing to the associated abrupt drop in resistance and the consistent transition pressure reported in the literature.[58,106]

The pressure dependence of the aluminum concentration in bridgmanite coexisting with corundum has recently been used to calibrate pressures above 26.5 GPa in multi-anvil presses.[39,42] However, the term "solubility of Al_2O_3 in bridgmanite" in the original papers can be ambiguous.[72,107,108] Here, we clarify that it refers specifically to the mole fraction of Al_2O_3 in bridgmanite within the $MgSiO_3$–Al_2O_3 binary end-member system [i.e., $MgSiO_{3(1-x)}$–$Al_2O_{3(x)}$] when in equilibrium with corundum phase.

We have reevaluated all published data[72,107–111] and have established a correlation for the Al_2O_3 mole percent (i.e., Al_2O_3 mol. %, defined as $xAl_2O_3 \times 100$) in bridgmanite within the $MgSiO_3$–Al_2O_3 binary end-member system as a function of pressure (26.6–51.8 GPa) and temperature (1673–3000 K), yielding the following relationship:

$$\begin{aligned} Al_2O_3(\text{mol. \%}) = {} & (0.675 \pm 0.047)P(\text{GPa}) \\ & + (0.016\,19 \pm 0.000\,81)T(\text{K}) \\ & - (37.9 \pm 2.6), \quad R^2 = 0.93. \end{aligned} \tag{30}$$

TABLE V. Mechanical properties of WC anvils used in this study.

Grade	Rockwell hardness HRA	Vickers hardness HV (kgf/mm^2)	Vickers hardness HV (GPa)[a]	Young's modulus (GPa)
ZK20A[b]	92.5[c]	1670[d]	16.4	⋯
JN08[e]	91.5[c]	1550[d]	15.2	⋯
GF35H[f]	91.2[c]	1520[d]	14.9	⋯
ZK10[b]	93.0[c]	1730[d]	17	⋯
	93.0[g]	1800[g]	17.7	⋯
ZK01[b]	93.5[c]	1820[d]	17.8	⋯
	93.5[g]	1900[g]	18.6	⋯
F05[h]	95.5[i]	2350[i]	23	600[i]
	⋯	⋯	24.1[j]	618 ± 2[k]
				600[l]
	⋯	2200[m]	21.6	610[m]
	95.1[n]	2140[d]	21	⋯
	95.0[g]	2400[g]	23.5	⋯

[a] HV(GPa) = HV(kgf/mm^2) × 0.009 806 65.
[b] Manufacturer: Heyuan Zhengxin Hardmetal Carbide Co., Ltd.
[c] Data from manufacturer's product manual.
[d] The HV value is derived from the conversion tables provided in DIN 50150:2000-10. For HRA values higher than 93.2, the corresponding HV value was estimated by extrapolation from the conversion table using the relationship HV(kgf/mm^2) = 200×HRA-16880.
[e] Manufacturer: Jinan Metallurgical Science Research Institute Co., Ltd.
[f] Manufacturer: Luoyang Golden Egret Geotools Co., Ltd.
[g] Data from Ref. 39.
[h] Manufacturer: Fuji Die Co., Ltd.
[i] Data from C006-3-23 (C-209CH) product manual.
[j] Data from Ref. 112.
[k] Data obtained by strain gauge method from Ref. 112.
[l] Data obtained by ultrasonic method from Ref. 112.
[m] Data from Ref. 33.
[n] Data from J006-17-22 (C-209) product manual.

This method requires careful control of starting materials, such as using reactive glass and adjusting compositions for limited bridgmanite grain growth. Further development of pressure calibrants above 26.5 GPa is needed for better constraints. Our run products show that the Al_2O_3 content in bridgmanite varies with grain size (Fig. 3), with a systematic decrease in aluminum as the grain size increases, likely due to sluggish intergranular diffusion or local disequilibrium. Brightness differences in BSE images exclude contamination from corundum during electron probe microanalysis (Fig. 3). For pressure calculations, we used compositions from the smallest, most equilibrium-like grains (<3 μm), which generally have comparably high Al_2O_3 contents, suggesting that our calculated pressures might be still underestimated.

VI. RECOMMENDATIONS FOR FUTURE EXPERIMENTS

Pressure calibration experiments on the large-volume presses at HPSTAR were conducted using a range of tungsten carbide anvil grades, including ZK20A, JN8, GF35H, ZK10, ZK01F, and F05, the hardness data for which are presented in Table V. These grades differ in mechanical properties such as hardness and Young's modulus. Even minor variations in anvil hardness can cause significant differences in the pressures generated for Kawai-type and Osugi-type multi-anvil presses,[33,112] leading to notable uncertainties. Accordingly, we strongly recommend that the equations presented above be applied only with the specific anvil grade for which they were developed.

Magnesium oxide (MgO) octahedra doped with 5 wt. % Cr_2O_3 (brown in color) were used for most of the pressure calibrations of the HPSTAR LVPs. Two other types of octahedra, pure MgO (white) and MgO doped with CoO (pink), are increasingly being adopted in different laboratories. While the limited data from this study indicate slightly lower pressure generation with the CoO-doped MgO octahedron, this is insufficient to clarify the detailed differences in performance among the three types. Therefore, we recommend avoiding their mixed use. Further studies are needed to evaluate the effects of different octahedron compositions on pressure generation.

Any changes to the materials used in a given assembly can influence pressure generation,[46,113] including variations in spacer and sleeve materials, each of which possesses distinct thermal and mechanical properties. For instance, sintered aluminum oxide (Al_2O_3) is sometimes used as a substitute for MgO in sleeves; however, the significant difference in bulk modulus between these materials may lead to variations in the pressure applied to samples in an LVP.[32,114] Additionally, the width of the pyrophyllite gaskets and their hydration state, whether fully or partially dehydroxylated, can also affect the pressure generated on the sample.[114,115] We therefore recommend using the assembly configurations given by Eqs. (13)–(26) exclusively with such gaskets to avoid significant deviations from the pressure calibration curves established in this study.

VII. CONCLUSION

We have established pressure calibration curves for nine LVPs at HPSTAR, encompassing piston–cylinder, cubic, and multi-anvil presses. By utilizing a range of well-characterized phase transitions and an empirical viscoplastic equation, we have achieved consistent and precise correlations between oil pressure and sample pressure. Our results have also revealed the factors that potentially influence calibration precision, including anvil properties, pressure transmission medium, and assembly design. This work thus provides a foundational reference for high-pressure experiments using LVPs at HPSTAR and offers practical guidance for similar experimental setups elsewhere, thereby enabling more consistent comparison of experimental results between different laboratories. This supports reproducible studies under extreme conditions relevant to Earth and planetary sciences, as well as advanced materials research.

SUPPLEMENTARY MATERIAL

Supplementary material A provides a compilation of published phase transition pressure data for the pressure markers used in this study. Supplementary material B details the procedures for data fitting with the Voce equation using Origin or OriginPro software.

ACKNOWLEDGMENTS

We thank Tomoo Katsura for his useful comments on the original manuscript and the two anonymous reviewers for their constructive comments and valuable contributions to the peer review of this work. This research was supported by the National Science Foundation of China (Grant Nos. U1530402 and U1930401).

AUTHOR DECLARATIONS

Conflict of Interest

The authors have no conflicts to disclose.

Author Contributions

Yongjiang Xu (徐永江): Data curation (equal); Formal analysis (equal); Investigation (equal); Methodology (equal); Validation (equal); Writing – original draft (equal); Writing – review & editing (equal). **Peiyan Wu (吴培衍)**: Data curation (equal); Formal analysis (equal); Investigation (equal); Methodology (equal); Validation (equal); Writing – original draft (equal); Writing – review & editing (equal). **Sheng Shang (尚升)**: Data curation (equal); Formal analysis (equal); Investigation (equal); Methodology (equal); Validation (equal); Writing – review & editing (equal). **Xue Wang (王雪)**: Data curation (equal); Formal analysis (equal); Investigation (equal); Methodology (equal); Validation (equal); Writing – review & editing (equal). **Taihang Li (李钛航)**: Data curation (equal); Formal analysis (equal); Investigation (equal); Methodology (equal); Validation (equal). **Shuchang Gao (高书畅)**: Data curation (equal); Formal analysis (equal); Investigation (equal); Methodology (equal); Validation (equal). **Shijie Lv (吕世杰)**: Data curation (equal); Investigation (equal); Methodology (equal); Validation (equal); Writing – review & editing (equal). **Hang Cheng (程行)**: Data curation (equal); Formal analysis (equal); Investigation (equal); Methodology (equal); Validation (equal); Writing – review & editing (equal). **Qianzhi Xu (许潜智)**: Data curation (equal); Formal analysis (equal); Investigation (equal); Methodology (equal); Validation (equal). **Shang Lei (雷尚)**: Data curation

(equal); Formal analysis (equal); Investigation (equal); Methodology (equal); Validation (equal). **Jiajia Feng (冯嘉嘉)**: Data curation (equal); Formal analysis (equal); Investigation (equal); Methodology (equal); Validation (equal). **Lei Zhao (赵磊)**: Data curation (equal); Formal analysis (equal); Investigation (equal); Methodology (equal); Validation (equal). **Wim van Westrenen**: Investigation (equal); Methodology (equal); Validation (equal); Writing – review & editing (equal). **Takayuki Ishii (石井貴之)**: Investigation (equal); Methodology (equal); Validation (equal); Writing – review & editing (equal). **Bin Chen (陈斌)**: Investigation (equal); Methodology (equal); Validation (equal); Writing – review & editing (equal). **Lei Su (苏磊)**: Investigation (equal); Methodology (equal); Validation (equal); Writing – review & editing (equal). **Yang Ding (丁阳)**: Investigation (equal); Methodology (equal); Validation (equal); Writing – review & editing (equal). **Wenge Yang (杨文革)**: Investigation (equal); Methodology (equal); Validation (equal); Writing – review & editing (equal). **Ho-Kwang Mao (毛河光)**: Investigation (equal); Methodology (equal); Validation (equal); Writing – review & editing (equal). **Yanhao Lin (林彦蒿)**: Conceptualization (equal); Investigation (equal); Methodology (equal); Project administration (equal); Validation (equal); Writing – review & editing (equal).

DATA AVAILABILITY

The data that support the findings of this study are available from the corresponding author upon reasonable request.

REFERENCES

[1]P. Bridgman, "General survey of certain results in the field of high-pressure physics," in *Nobel Lecture* (Elsevier Publishing Company, 1946).

[2]B. Chen, "Exploring nanomechanics with high-pressure techniques," Matter Radiat. Extremes **5**, 068104 (2020).

[3]H. T. Hall, "Ultrahigh-pressure research: At ultrahigh pressures new and sometimes unexpected chemical and physical events occur," Science **128**, 445–449 (1958).

[4]T. Ishii and E. Ohtani, "Dry metastable olivine and slab deformation in a wet subducting slab," Nat. Geosci. **14**, 526–530 (2021).

[5]J. Kong, K. Shi, A. R. Oganov, J. Zhang, L. Su *et al.*, "Exotic compounds of monovalent calcium synthesized at high pressure," Matter Radiat. Extremes **9**, 067803 (2024).

[6]Y. Lin, E. J. Tronche, E. S. Steenstra, and W. Van Westrenen, "Evidence for an early wet moon from experimental crystallization of the lunar magma ocean," Nat. Geosci. **10**, 14–18 (2017).

[7]H.-K. Mao and R. J. Hemley, "The high-pressure dimension in Earth and planetary science," Proc. Natl. Acad. Sci. U. S. A. **104**, 9114 (2007).

[8]H.-K. Mao, "Hydrogen and related matter in the pressure dimension," Matter Radiat. Extremes **7**, 063001 (2022).

[9]H.-K. Mao, Q. Hu, L. Yang, J. Liu, D. Y. Kim *et al.*, "When water meets iron at Earth's core–mantle boundary," Natl. Sci. Rev. **4**, 870–878 (2017).

[10]H.-K. Mao, X.-J. Chen, Y. Ding, B. Li, and L. Wang, "Solids, liquids, and gases under high pressure," Rev. Mod. Phys. **90**, 015007 (2018).

[11]H.-K. Mao, B. Chen, H. Gou, K. Li, J. Liu *et al.*, "2022 HP special volume: Interdisciplinary high pressure science and technology," Matter Radiat. Extremes **8**, 063001 (2023).

[12]H. Tang, X. Yuan, Y. Cheng, H. Fei, F. Liu *et al.*, "Synthesis of paracrystalline diamond," Nature **599**, 605–610 (2021).

[13]R. Tao and Y. Fei, "High-pressure experimental constraints of partitioning behavior of Si and S at the Mercury's inner core boundary," Earth Planet Sci. Lett. **562**, 116849 (2021).

[14]Y. Xu, Y. Lin, P. Wu, O. Namur, Y. Zhang *et al.*, "A diamond-bearing core-mantle boundary on Mercury," Nat. Commun. **15**, 5061 (2024).

[15]L. Zhang, Y. Wang, J. Lv, and Y. Ma, "Materials discovery at high pressures," Nat. Rev. Mater. **2**, 17005–17016 (2017).

[16]J. Zhao, J. Gao, W. Li, Y. Qian, X. Shen *et al.*, "A combinatory ferroelectric compound bridging simple ABO_3 and A-site-ordered quadruple perovskite," Nat. Commun. **12**, 747 (2021).

[17]L. Duan, J. Zhang, X. Wang, J. Zhao, L. Cao *et al.*, "High-pressure synthesis, structure and properties of new ternary pnictides La_3TiX_5 (X = P, As)," J. Alloys Compd. **831**, 154697 (2020).

[18]H.-K. Mao, B. Chen, J. Chen, K. Li, J. F. Lin *et al.*, "Recent advances in high-pressure science and technology," Matter Radiat. Extremes **1**, 59–75 (2016).

[19]P. F. McMillan, "New materials from high-pressure experiments," Nat. Mater. **1**, 19–25 (2002).

[20]H. Tang, X. Yuan, P. Yu, Q. Hu, M. Wang *et al.*, "Revealing the formation mechanism of ultrahard nanotwinned diamond from onion carbon," Carbon **129**, 159–167 (2018).

[21]F. R. Boyd and J. L. England, "Apparatus for phase-equilibrium measurements at pressures up to 50 kilobars and temperatures up to 1750 °C," J. Geophys. Res. **65**, 741–748, https://doi.org/10.1029/jz065i002p00741 (1960).

[22]P. McDade, B. J. Wood, W. Van Westrenen, R. Brooker, G. Gudmundsson *et al.*, "Pressure corrections for a selection of piston-cylinder cell assemblies," Mineral. Mag. **66**, 1021–1028 (2002).

[23]X. Liu, J. Chen, J. Tang, Q. He, S. Li *et al.*, "A large volume cubic press with a pressure-generating capability up to about 10 GPa," High Press. Res. **32**, 239–254 (2012).

[24]D. Frost, B. Poe, R. Trønnes, C. Liebske, A. Duba *et al.*, "A new large-volume multianvil system," Phys. Earth Planet. Inter. **143**, 507–514 (2004).

[25]F. B. Hua, K.-C. Liang, J. Kung, W.-L. Hsu, and Y. Wang, "A large volume multi-anvil apparatus for the Earth sciences community in Taiwan," Terr. Atmos. Oceanic Sci. **23**, 647–655 (2012).

[26]N. Kawai and S. Endo, "The generation of ultrahigh hydrostatic pressures by a split sphere apparatus," Rev. Sci. Instrum. **41**, 1178–1181 (1970).

[27]N. Kawai, "A static high pressure apparatus with tapering multi-pistons forming a sphere. I," Proc. Jpn. Acad. **42**, 385–388 (1966).

[28]J. Osugi, K. Shimizu, K. Inoue, and K. Yasunami, "A compact cubic anvil high pressure apparatus," Rev. Phys. Chem. Jpn. **34**, 1–6 (1964), see http://hdl.handle.net/2433/46842.

[29]D. Walker, M. Carpenter, and C. Hitch, "Some simplifications to multianvil devices for high pressure experiments," Am. Mineral. **75**, 1020–1028 (1990).

[30]R. Farla, "Towards joint *in situ* determination of pressure and temperature in the large volume press exclusively from X-ray diffraction," J. Synchrotron Radiat. **30**, 807–814 (2023).

[31]X. Hou, Y. Shang, L. Chen, B. Feng, Y. Zhao *et al.*, "Ultrahigh pressure generation at high temperatures in a Walker-type large-volume press and multiple applications," Engineering **45**, 155–164 (2025).

[32]T. Ishii, L. Shi, R. Huang, N. Tsujino, D. Druzhbin *et al.*, "Generation of pressures over 40 GPa using Kawai-type multi-anvil press with tungsten carbide anvils," Rev. Sci. Instrum. **87**, 024501 (2016).

[33]T. Ishii, D. Yamazaki, N. Tsujino, F. Xu, Z. Liu *et al.*, "Pressure generation to 65 GPa in a Kawai-type multi-anvil apparatus with tungsten carbide anvils," High Pressure Res. **37**, 507–515 (2017).

[34]T. Ishii, Z. Liu, and T. Katsura, "A breakthrough in pressure generation by a Kawai-type multi-anvil apparatus with tungsten carbide anvils," Engineering **5**, 434–440 (2019).

[35]J. Knibbe, S. Luginbühl, R. Stoevelaar, W. Van der Plas, D. Van Harlingen *et al.*, "Calibration of a multi-anvil high-pressure apparatus to simulate planetary interior conditions," EPJ Tech. Instrum. **5**, 5 (2018).

[36]R. C. Liebermann, "My research collaborations with Chinese scientists over the past three decades," Int. J. Geosci. **12**, 960–983 (2021).

[37]M. Masotta, C. Freda, T. Paul, G. Moore, M. Gaeta *et al.*, "Low pressure experiments in piston cylinder apparatus: Calibration of newly designed 25 mm furnace assemblies to P = 150 MPa," Chem. Geol. **312**, 74–79 (2012).

[38]G. Moore, K. Roggensack, and S. Klonowski, "A low-pressure high-temperature technique for the piston-cylinder," Am. Mineral. **93**, 48–52 (2008).

[39]Y.-C. Shang, F.-R. Shen, X.-Y. Hou, L.-Y. Chen, K. Hu *et al.*, "Pressure generation above 35 GPa in a walker-type large-volume press," Chin. Phys. Lett. **37**, 080701 (2020).
[40]S. R. F. Vlach, A. F. Salazar-Naranjo, J. S. Torres-Corredor, P. R. d. Carvalho, and G. Mallmann, "Calibration of high-temperature furnace assemblies for experiments between 200 and 600 MPa with end-loaded piston-cylinder apparatuses," Braz. J. Geol. **49**, e20180090 (2019).
[41]D. Walker and J. Li, "Castable solid pressure media for multianvil devices," Matter Radiat. Extremes **5**, 018402 (2020).
[42]X. Zhao, F. Ren, J. He, Y. Pan, H. Tang *et al.*, "Ultrahigh-pressure generation above 50 GPa in a Kawai-type large-volume press," Matter Radiat. Extremes **10**, 047801 (2025).
[43]D. L. Decker, "High-pressure equation of state for NaCl, KCl, and CsCl," J. Appl. Phys. **42**, 3239–3244 (1971).
[44]Y. Tange, Y. Nishihara, and T. Tsuchiya, "Unified analyses for *P-V-T* equation of state of MgO: A solution for pressure-scale problems in high *P-T* experiments," J. Geophys. Res.: Solid Earth **114**, B03208, https://doi.org/10.1029/2008JB005813 (2009).
[45]M. Yokoo, N. Kawai, K. G. Nakamura, K.-i. Kondo, Y. Tange *et al.*, "Ultrahigh-pressure scales for gold and platinum at pressures up to 550 GPa," Phys. Rev. B **80**, 104114 (2009).
[46]K. D. Leinenweber, J. A. Tyburczy, T. G. Sharp, E. Soignard, T. Diedrich *et al.*, "Cell assemblies for reproducible multi-anvil experiments (the COMPRES assemblies)," Am. Mineral. **97**, 353–368 (2012).
[47]K. Bose and J. Ganguly, "Quartz-coesite transition revisited: Reversed experimental determination at 500–1200 °C and retrieved thermochemical properties," Am. Mineral. **80**, 231–238 (1995).
[48]M. Akaogi, *High-Pressure Silicates and Oxides* (Springer Nature, Singapore, 2022).
[49]V. Bean, S. Akimoto, P. Bell, S. Block, W. Holzapfel *et al.*, "Another step toward an international practical pressure scale: 2nd AIRAPT IPPS task group report," Physica B+C **139**, 52–54 (1986).
[50]D. L. Decker, W. A. Bassett, L. Merrill, H. T. Hall, and J. D. Barnett, "High-pressure calibration: A critical review," J. Phys. Chem. Ref. Data **1**, 773–836 (1972).
[51]E. Ito, G. Price, and G. Schubert, "Theory and practice-multianvil cells and high-pressure experimental methods," Treatise Geophys. **2**, 197–230 (2007).
[52]E. Ito, "Multi-anvil cells and high pressure experimental methods," Treatise Geophys. **2**, 233–261 (2015).
[53]P. Bridgman, *The Physics of High Pressure* (G. Bell and Sons, Ltd., London, 1931).
[54]P. L. M. Heydemann, "Erratum: The Bi I-II transition pressure measured with a dead-weight piston gauge," J. Appl. Phys. **38**, 3424 (1967).
[55]M. Huang, F. Peng, S. Guan, J. Zhang, W. Liang *et al.*, "Powder conductor for pressure calibration applied to large volume press under high pressure," Rev. Sci. Instrum. **92**, 073903 (2021).
[56]G. Andersson, B. Sundqvist, and G. Bäckström, "A high-pressure cell for electrical resistance measurements at hydrostatic pressures up to 8 GPa: Results for Bi, Ba, Ni, and Si," J. Appl. Phys. **65**, 3943–3950 (1989).
[57]S. Ono, "High-pressure phase transition of bismuth," High Pressure Res. **38**, 414–421 (2018).
[58]S. Ono, "Phase transition in ZnSe at high pressures and high temperatures," J. Phys. Chem. Solid. **141**, 109409 (2020).
[59]A. Ohtani, S. Mizukami, M. Katayama, A. Onodera, and N. Kawai, "Multi-anvil apparatus for high pressure X-ray diffraction," Jpn. J. Appl. Phys. **16**, 1843 (1977).
[60]S. Ono and T. Kikegawa, "Phase transformation of GaAs at high pressures and temperatures," J. Phys. Chem. Solid. **113**, 1–4 (2018).
[61]S. Ono and T. Kikegawa, "Determination of the phase boundary of GaP using in situ high pressure and high-temperature X-ray diffraction," High Pressure Res. **37**, 28–35 (2017).
[62]C. Hejny and M. I. McMahon, "Large structural modulations in incommensurate Te-III and Se-IV," Phys. Rev. Lett. **91**, 215502 (2003).
[63]J. Akella, S. N. Vaidya, and G. C. Kennedy, "Melting of sodium chloride at pressures to 65 kbar," Phys. Rev. **185**, 1135 (1969).
[64]S. Ono, T. Kikegawa, Y. Higo, and Y. Tange, "Precise determination of the phase boundary between coesite and stishovite in SiO_2," Phys. Earth Planet. Inter. **264**, 1–6 (2017).
[65]S. Ono, T. Kikegawa, and Y. Higo, "*In situ* observation of a phase transition in Fe_2SiO_4 at high pressure and high temperature," Phys. Chem. Miner. **40**, 811–816 (2013).
[66]T. Katsura, H. Yamada, O. Nishikawa, M. Song, A. Kubo *et al.*, "Olivine-wadsleyite transition in the system $(Mg, Fe)_2SiO_4$," J. Geophys. Res.: Solid Earth **109**, B02209, https://doi.org/10.1029/2003JB002438 (2004).
[67]T. Inoue, T. Irifune, Y. Higo, T. Sanehira, Y. Sueda *et al.*, "The phase boundary between wadsleyite and ringwoodite in Mg_2SiO_4 determined by *in situ* X-ray diffraction," Phys. Chem. Miner. **33**, 106–114 (2006).
[68]A. Chanyshev, T. Ishii, D. Bondar, S. Bhat, E. J. Kim *et al.*, "Depressed 660-km discontinuity caused by akimotoite–bridgmanite transition," Nature **601**, 69–73 (2022).
[69]Y. Singh, "Electrical resistivity measurements: A review," Int. J. Mod. Phys.: Conf. Ser. **22**, 745–756 (2013).
[70]T. Ishii, N. Miyajima, G. Criniti, Q. Hu, K. Glazyrin *et al.*, "High pressure-temperature phase relations of basaltic crust up to mid-mantle conditions," Earth Planet Sci. Lett. **584**, 117472 (2022).
[71]T. Katsura, "Phase relations of bridgmanite, the most abundant mineral in the Earth's lower mantle," Commun. Chem. **8**, 28 (2025).
[72]Z. Liu, T. Irifune, M. Nishi, Y. Tange, T. Arimoto *et al.*, "Phase relations in the system $MgSiO_3$–Al_2O_3 up to 52 GPa and 2000 K," Phys. Earth Planet. Inter. **257**, 18–27 (2016).
[73]L. Gibson and M. F. Ashby, *Cellular Solids Structure and Properties* (Cambridge University Press, Cambridge, 1997).
[74]L. J. Gibson, "Cellular solids," MRS Bull. **28**, 270–274 (2003).
[75]D. Schulze, *Powders and Bulk Solids: Behavior, Characterization, Storage and Flow* (Springer-Verlag, Berlin, Heidelberg, 2008).
[76]J. Betten, *Creep Mechanics* (Springer-Verlag, Berlin, Heidelberg, 2008).
[77]J. Lubliner, *Plasticity Theory* (Macmillan Publishing Company, New York, 1990).
[78]P. Perzyna, "Fundamental problems in viscoplasticity," Adv. Appl. Mech. **9**, 243–377 (1966).
[79]J. Poirier, *Creep of Crystals: High-Temperature Deformation Processes in Metals, Ceramics and Minerals* (Cambridge University Press, 1985).
[80]M. F. Ashby, "The deformation of plastically non-homogeneous materials," Philos. Mag.: A J. Theor. Exp. Appl. Phys. **21**, 399–424 (1970).
[81]G. Dieter, *Mechanical Metallurgy* (McGraw-Hill Book Company, 1961).
[82]W. Findley, J. S. Lai, and K. Onaran, *Creep and Relaxation of Nonlinear Viscoelastic Materials* (Dover Publications, Inc., New York, 1976).
[83]T. G. Langdon, "Grain boundary sliding revisited: Developments in sliding over four decades," J. Mater. Sci. **41**, 597–609 (2006).
[84]M. Meyers and K. Chawla, *Mechanical Behavior of Materials* (Cambridge University Press, 2008).
[85]Y. Estrin and H. Mecking, "A unified phenomenological description of work hardening and creep based on one-parameter models," Acta Metall. **32**, 57–70 (1984).
[86]U. F. Kocks and H. Mecking, "Physics and phenomenology of strain hardening: The FCC case," Prog. Mater. Sci. **48**, 171–273 (2003).
[87]H. Mecking and U. F. Kocks, "Kinetics of flow and strain-hardening," Acta Metall. **29**, 1865–1875 (1981).
[88]R. Hill, *The Mathematical Theory of Plasticity* (Oxford University Press, 1998).
[89]J. H. Palm, "Stress-strain relations for uniaxial loading," Flow, Turbul. Combust. **1**, 198–214 (1949).
[90]E. Voce, "The relationship between stress and strain for homogeneous deformation," J. Inst. Met. **74**, 537–562 (1948).
[91]E. Voce, "A practical strain hardening function," Metallurgia **51**, 219–226 (1955).
[92]P. Wu, Y. Xu, and Y. Lin, "A novel rapid cooling assembly design in a high-pressure cubic press apparatus," Matter Radiat. Extremes **9**, 027402 (2024).
[93]O. Degtyareva, M. I. McMahon, and R. J. Nelmes, "High-pressure structural studies of group-15 elements," High Pressure Res. **24**, 319–356 (2004).

[94]S. Ono and T. Kikegawa, "Phase transition of ZnS at high pressures and temperatures," Phase Transitions **91**, 9–14 (2018b).
[95]S. Desgreniers, L. Beaulieu, and I. Lepage, "Pressure-induced structural changes in ZnS," Phys. Rev. B **61**, 8726 (2000).
[96]G. A. Samara and H. G. Drickamer, "Pressure induced phase transitions in some II–VI compounds," J. Phys. Chem. Solid. **23**, 457–461 (1962).
[97]J. Z. Jiang, L. Gerward, D. Frost, R. Secco, J. Peyronneau *et al.*, "Grain-size effect on pressure-induced semiconductor-to-metal transition in ZnS," J. Appl. Phys. **86**, 6608–6610 (1999).
[98]S. B. Qadri, E. F. Skelton, A. D. Dinsmore, J. Z. Hu, W. J. Kim *et al.*, "The effect of particle size on the structural transitions in zinc sulfide," J. Appl. Phys. **89**, 115–119 (2001).
[99]Y. Ge, S. Ma, C. You, K. Hu, C. Liu *et al.*, "A distinctive HPHT platform with different types of large-volume press subsystems at SECUF," Matter Radiat. Extremes **9**, 063801 (2024).
[100]K. Hu, R. Liu, S. Liu, B. Feng, S. Wang *et al.*, "A rapid compression large-volume press with a high pressure jump above 10 GPa within milliseconds," Rev. Sci. Instrum. **95**, 103905 (2024).
[101]D. Ren and H. Li, "Pressure calibration of large-volume press: A case study of hinged 6–8 type large-volume high-pressure apparatus," Front. Earth Sci. **10**, 851813 (2022).
[102]A. Onodera, A. Ohtani, S. Tsuduki, and O. Shimomura, "Synchrotron X-ray diffraction study of ZnTe at high pressure," Solid State Commun. **145**, 374–378 (2008).
[103]X. Cui, T. Hu, J. Yang, Y. Han, Y. Li *et al.*, "The electrical properties of ZnTe under high pressure and moderate temperature," Phys. Status Solidi C **8**, 1676–1679 (2011).
[104]A. Ohtani, M. Motobayashi, and A. Onodera, "Polymorphism of ZnTe at elevated pressure," Phys. Lett. **75**, 435–437 (1980).
[105]S. V. Ovsyannikov and V. V. Shchennikov, "Phase transitions investigation in ZnTe by thermoelectric power measurements at high pressure," Solid State Commun. **132**, 333–336 (2004).
[106]S. R. Tiong, M. Hiramatsu, Y. Matsushima, and E. Ito, "The phase transition pressures of zincsulfoselenide single crystals," Jpn. J. Appl. Phys. **28**, 291–292 (1989).
[107]A. Kubo and M. Akaogi, "Post-garnet transitions in the system $Mg_4Si_4O_{12}$–$Mg_3Al_2Si_3O_{12}$ up to 28 GPa: Phase relations of garnet, ilmenite and perovskite," Phys. Earth Planet. Inter. **121**, 85–102 (2000).
[108]Z. Liu, M. Nishi, T. Ishii, H. Fei, N. Miyajima *et al.*, "Phase relations in the system $MgSiO_3$–Al_2O_3 up to 2300 K at lower mantle pressures," J. Geophys. Res.: Solid Earth **122**, 7775–7788, https://doi.org/10.1002/2017jb014579 (2017).
[109]T. Irifune, T. Koizumi, and J.-i. Ando, "An experimental study of the garnet-perovskite transformation in the system $MgSiO_3$–$Mg_3Al_2Si_3O_{12}$," Phys. Earth Planet. Inter. **96**, 147–157 (1996).
[110]Z. Liu, R. Liu, Y. Shang, F. Shen, L. Chen *et al.*, "Aluminum solubility in bridgmanite up to 3000 K at the top lower mantle," Geosci. Front. **12**, 929–935 (2021).
[111]L. Wang, Z. Liu, S. Koizumi, T. B. Ballaran, and T. Katsura, "Aluminum components in bridgmanite coexisting with corundum and the CF-Phase with temperature," J. Geophys. Res.: Solid Earth **128**, e2022JB025739, https://doi.org/10.1029/2022jb025739 (2023).
[112]K. Wada, T. Yagi, H. Gotou, R. Iizuka, M. Kawakami *et al.*, "Development of new WC-Ni hardmetals for use in high pressure experiments," High Press. Res. **35**, 123–139 (2015).
[113]A. Shatskiy, T. Katsura, K. D. Litasov, A. V. Shcherbakova, Y. M. Borzdov *et al.*, "High pressure generation using scaled-up Kawai-cell," Phys. Earth Planet. Inter. **189**, 92–108 (2011).
[114]N. Soga and O. Anderson, "High-temperature elastic properties of polycrystalline MgO and Al_2O_3," J. Am. Ceram. Soc. **49**, 355–359 (1966).
[115]A. J. Stewart, W. Van Westrenen, M. W. Schmidt, and E. Melekhova, "Effect of gasketing and assembly design: A novel 10/3.5 mm multi-anvil assembly reaching perovskite pressures," High Pressure Res. **26**, 293–299 (2006).